Creating an Archaeomagnetic Dating Curve for Minnesota: Assessing the potential of Minnesota ceramic sherds to accurately record field intensity

A THESIS

SUBMITTED TO THE FACULTY OF THE GRADUATE SCHOOL

OF THE UNIVERSITY OF MINNESOTA

BY

Declan Ramirez

IN PARTIAL FULFILLMENT OF THE REQUIREMENTS

FOR THE DEGREE OF

MASTER OF SCIENCE

Joshua Feinberg and Maxwell Brown

May, 2024

Acknowledgments

We thank the Minnesota Historical Society, the University of Minnesota Earth and Environmental Sciences Department, the Science Museum of Minnesota, the Pedersen family, the Lower and Upper Sioux Indian communities, and the Prairie Island Indian community, without whom this project would not be possible. This work was performed at the Institute for Rock Magnetism (IRM) at the University of Minnesota. The IRM is a US National Multi-user Facility supported through the Instrumentation and Facilities program of the National Science Foundation, Earth Sciences Division (EAR-2153786), and by funding from the University of Minnesota. We thank Peat Solheid for laboratory assistance. Additionally, parts of this work were carried out in the Characterization Facility, University of Minnesota, which receives partial support from the NSF through the MRSEC (Award Number DMR-2011401) and the NNCI (Award Number ECCS-2025124) programs. We thank Nick Seaton for his expertise and assistance using the SEM. We also thank Ed Fleming, Mara Taft, and the Pedersen archaeological team for their efforts in securing the material used for this study, and the expertise of both the Pedersen archaeological team and the University of Minnesota Anthropology Department in characterizing the sherds used in this project.

Furthermore, we acknowledge that the University of Minnesota is built on the ancestral lands of the Wahpekute band that was ceded to the United States by the Treaty of Traverse des Sioux in July of 1851, in an agreement that was not paid in full and whose underlying aim was the dissolution of the Dakota culture. The University has also benefited from Chippewa and Dakota (Mede-wakanton, Wahpekuta, Wahpeton and Sisseton Bands) land ceded by treaty and given to the University of Minnesota via the Morrill Act. Due to its land-grant status, the

infrastructure, financial foundations, and faculty, students, and staff at the University of Minnesota all continue to benefit directly from these ceded lands, and we wish to acknowledge this support in our research.

Abstract

Precise dating of heat treated Minnesota artifacts is hampered by a scarcity of material suitable for radiocarbon dating, and uncertainties in stylistic dating of material culture (often > ± 500 years). Archaeomagnetic dating has the potential to refine the ages of nondiagnostic ceramics and other heated artifacts, but has not been implemented in Minnesota, as the region lacks a well-constrained reference curve. For this study, we analyze a collection of 21 ceramic sherds with differing material characteristics and ages, representative of the kinds of ceramics commonly found in southwest Minnesota. We performed rock magnetic analyses to better characterize the sherds, determining that the majority of specimens contain a range of magnetic grain sizes and compositions (magnetite/maghemite, goethite, and hematite). Archaeointensity experiments based on the IZZI method were encouraging, with approximately 86% of specimens showing promise under a modified version of the SELCRIT2 selection criteria. These results indicate that the construction of an archaeomagnetic reference curve for Minnesota (MARC) is feasible, and can be used as a tool to better constrain archaeological dates and the geomagnetic field in the state and surrounding area. Future work on this topic will deal with populating the MARC using archaeointensities and available radiocarbon dates.

Table of Contents

List of Tables

List of Figures

1. Introduction

Variations of Earth's magnetic field on archaeological timescales and the ability of fired archaeological materials to record these changes form the basis of archaeomagnetic dating. During firing of archaeological materials to high temperature, magnetic minerals within the source material can acquire a thermoremanent magnetization (TRM) on cooling below their Curie temperatures, preserving a snapshot of the past strength (intensity) and direction of the Earth's magnetic field. Laboratory measurements on fired materials (e.g., ceramics, hearths, soils, and kilns) can recover the past magnetic field, and when multiple recordings are obtained, they can be used in tandem with dates (e.g., historical, material culture, and/or radiocarbon) to create an archaeomagnetic reference curve (ARC). ARCs have been successfully established and used to date archaeological materials in Europe and the Middle East (e.g., Batt et al., 2017, Stillinger et al., 2015), but have yet to be applied to the United States' Midwest.

For this study, we assess the feasibility for an ARC to be created for Minnesota, where the ability to precisely date fired archaeological material is limited by the scarcity of material suitable for radiocarbon dating and the uncertainties in stylistic dating of material culture (often > ± 500 years). Archaeomagnetic dating is an alternative way to date archaeological material that addresses these limitations and can be established using the many ceramic sherds found in Minnesota, which would provide strong time resolution for the last 2,500 years or so that ceramics have been in production in Minnesota. However, before the ARC can be created it is necessary to assess the archaeomagnetic quality of the ceramic sherds that would be used to generate the curve. Here, we show that Minnesota ceramics are composed of a range of magnetic grain sizes and compositions (magnetite/maghemite, goethite, and hematite), and that

approximately 86% of our sherds show promise for the establishment of an ARC in Minnesota. These results indicate that the construction of an archaeomagnetic reference curve for Minnesota (MARC) is feasible, and can be used as a tool to better constrain archaeological dates and the geomagnetic field in the state and surrounding area.

2. Archaeological Setting and Specimens

2.1. Minnesota Ceramic Traditions and Sampled Potteries

For this study, we analyzed 21 ceramic sherds excavated from the Pedersen site (21LN02) in southwestern Minnesota (Figure 1). Sherds from this site were chosen specifically to provide a broad range of ceramic types and periods so that Minnesota ceramics as a whole could be assessed for archaeointensity suitability. Additionally, each sherd is presumed to be from a separate vessel. This collection features a variety of tempers, decorations, and exterior treatments, including both rim and body sherds (Figure 2) spanning the Woodland to Late Precontact periods (500 BCE - 1650 CE). In Minnesota, the Woodland period is associated with the start of widespread ceramic production by Indigenous peoples. Archaeologists often group ceramics into types and phases within a region based on similarities in design and construction, with these groupings typically corresponding with assumptions about chronological positions and ceramic developmental sequences.

At the Pedersen site and in our collection of sherds, the Fox Lake (Initial Woodland), Temperance Lake (Transitional Woodland), and Lake Benton (Late Woodland) phases are represented, as well as the more widespread Late Precontact traditions (Oneota and possibly Sandy Lake). The approximate time spans of these ceramic phases is as follows: Fox Lake (ca. 400 - 100 BCE), Temperance Lake (ca. 100 BCE - 400 CE), Lake Benton (ca. 700 - 1200/1300 CE), and Late Precontact (1300 - 1650 CE). The Fox Lake and Temperance Lake age ranges are estimates from Holley (2023), and the Lake Benton age range is from Anfinson (1997).

Four of the sherds in this collection are nondiagnostic, meaning they do not have design attributes that could be assigned to a type or mode category (ceramic phase), though they have

been given potential broader periods as their likely age ranges. Nondiagnostic sherds are given the following tentative age ranges based on their most likely time period, using ranges from Gibbon (2012): Initial or Middle Woodland (500 BCE - 500 CE), Late Woodland (500 CE - 1300 CE). Additionally, one sherd has a style/type designation, but no determined ceramic phase or likely age range provided, so it was given a range that spans the entirety of ceramic tradition in Minnesota (500 BCE - 1650 CE). Age ranges and sherd material characteristics are in Table 1. Sherds were selected and deaccessioned for destructive analysis at the Science Museum of Minnesota (SMM).

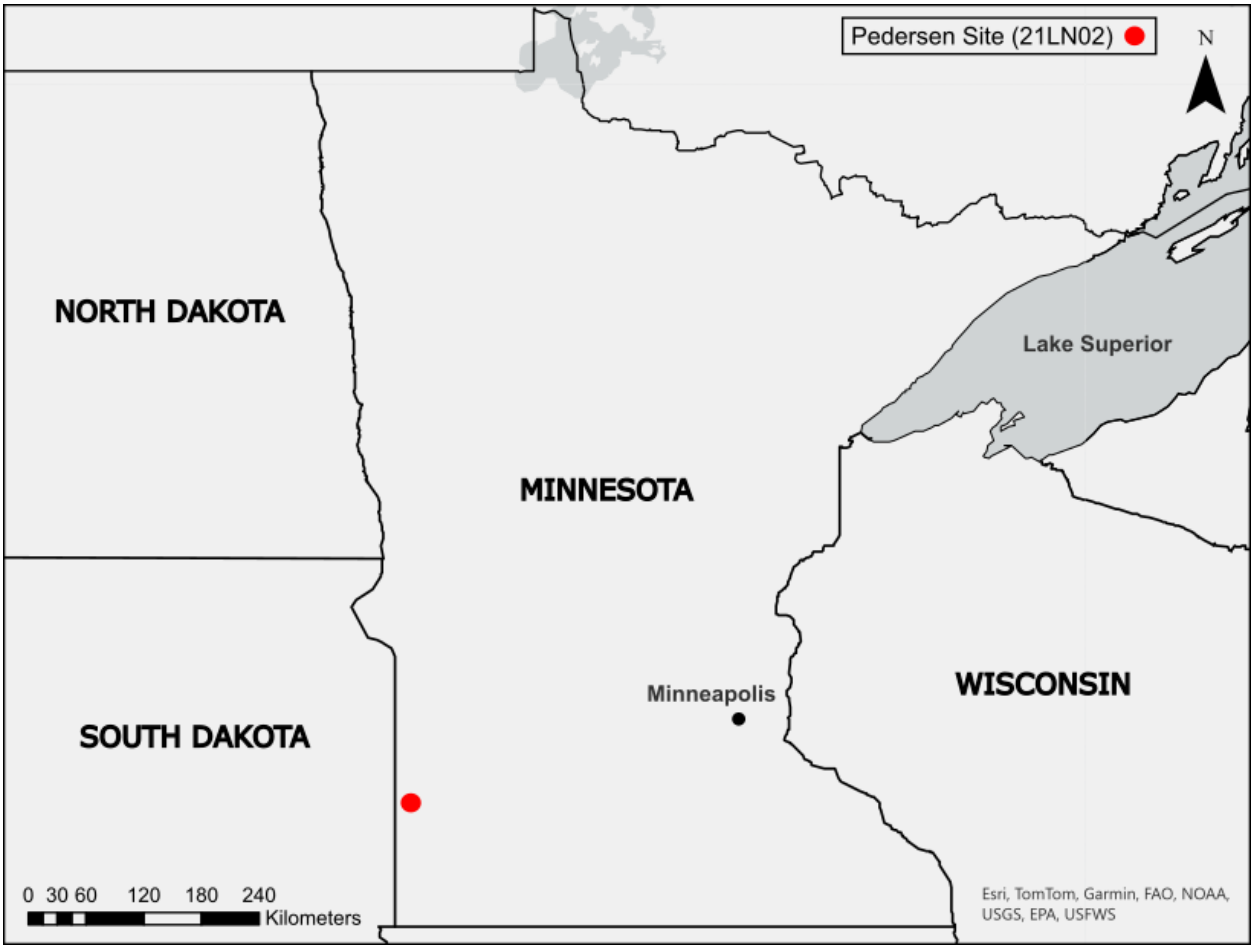

Figure 1. Approximate locations of southern Minnesota study sites sherds were sourced from.

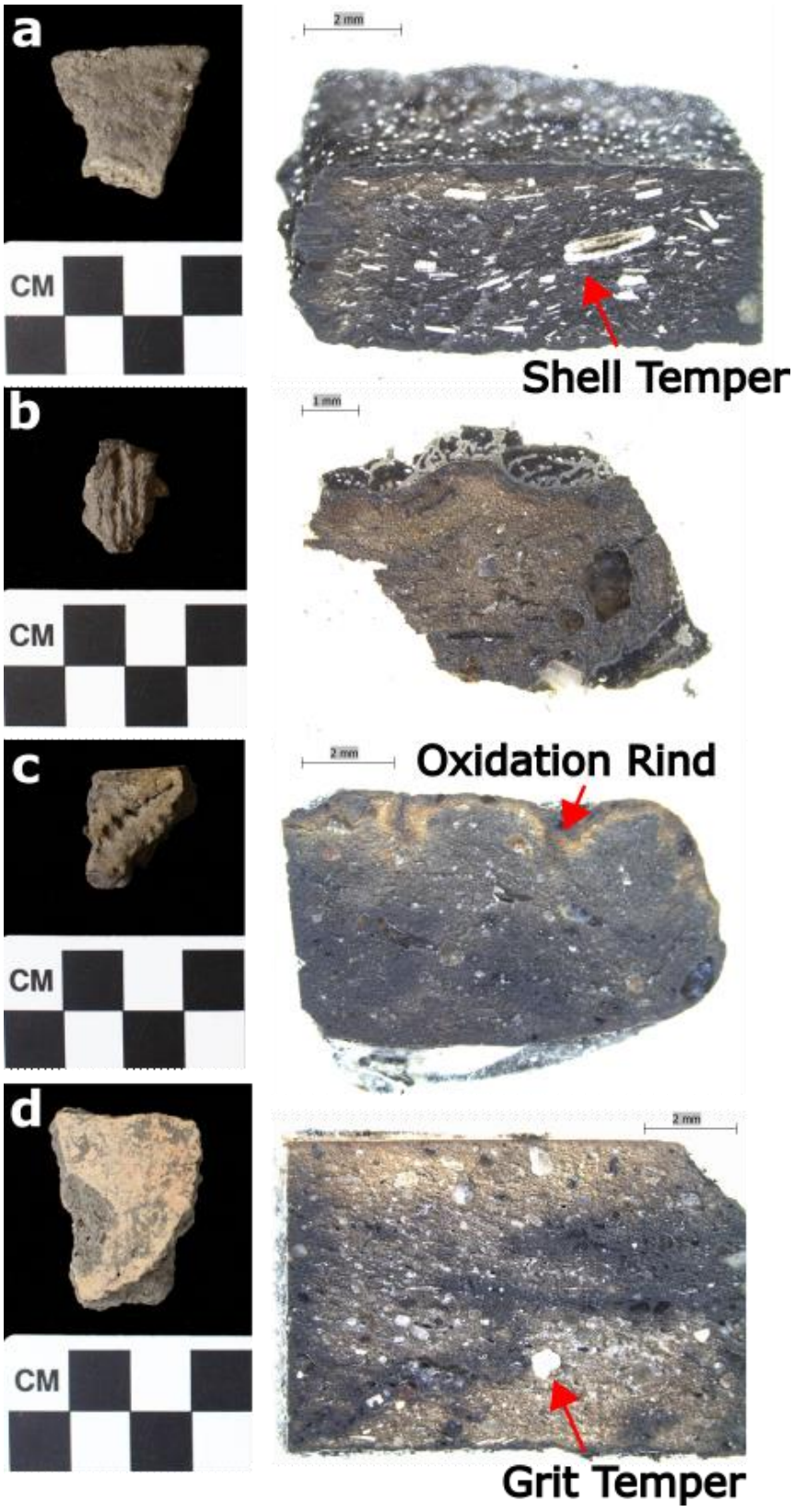
a
CM
2 mm
Shell Temper
b
CM
1 mm
c
CM
2 mm
Oxidation Rind
d
CM
2 mm
Grit Temper

Figure 2. Selection of sherds with representative material characteristics used in this study. (a) Shell tempered body sherd with exterior cordmarking (faint), possible Sandy Lake phase. (b) Grit tempered rim sherd with exterior cordmarking, Lake Benton phase. (c) Grit tempered rim sherd with plain exterior treatment and cordwrapped stick impressed decoration, Temperance Lake phase. (d) Grit tempered body sherd with plain exterior treatment, non-diagnostic, but likely Transitional Woodland.

3. Materials and Methods

Sherds (samples) were subdivided into 4 fragments (specimens) using a Buehler IsoMet Low Speed Saw, and weighed using a digital scale. The average mass of specimens was around 640 mg, and the average thickness around 6.7 mm (Table 1). When not being analyzed, specimens were stored within a shielded room at the Institute for Rock Magnetism (IRM), which attenuates the background magnetic field to around 200 nT (Bowles in IRM Quarterly 18-3).

3.1. Rock Magnetic Analyses

Specimens were subjected to a suite of rock magnetic measurements, including alternating field (AF) demagnetization, magnetic hysteresis, and low-temperature experiments. Prior to these treatments, a single magnetic susceptibility measurement was taken for each specimen using a Magnon Variable Frequency Susceptibility Meter (VFSM) in a field of 300 A/m at a frequency of 50 Hz. The natural remanent magnetization (NRM) and partial thermal remanent magnetization (pTRM) of the samples was measured using a 2G 755 Long Core DC SQUID magnetometer (‘the 2G’). Anhysteretic remanent magnetization (ARM) was applied using the D2000 DTech Precision Instruments AF (de)magnetizer (‘the DTech’). All rock magnetic measurements were made using equipment at the IRM, with the exception of scanning electron microscopy (SEM) and energy dispersive spectroscopy (EDS) analysis, which was completed at the University of Minnesota (UMN) Characterization Facility (CharFac).

3.1.1. Magnetic Hysteresis and FORCs

Room temperature hysteresis loops, first order reversal curves (FORCs), and backfield curves were measured on a Lake Shore 8600 Vibrating Sample Magnetometer (VSM). Hysteresis loops test a sample's ability to be affected by a changing magnetic field, which can be diagnostic of grain size. They provide useful parameters like saturation magnetization (Ms), saturation remanent magnetization (Mrs), and coercive force (Bc). Backfield curves generate the coercivity of remanence (Bcr), hard isothermal remanent magnetization (HIRM; Equation 1), and S-ratio (Equation 2) parameters. In samples containing magnetite and maghemite, the HIRM is a measure of the sample's absolute concentration of hematite and/or goethite (see Liu et al., 2007). The S-ratio can show relative abundance variations in low and high coercivity minerals, with values approaching one indicating that low coercivity minerals like magnetite and maghemite magnetically dominate the sample. Values near zero indicate that hematite and/or goethite may instead be the dominant magnetic mineral in the assemblage (see Liu et al., 2007).

FORC diagrams (Roberts et al., 2000) are another way to visualize hysteresis data using partial hysteresis curves (first order reversal curves). We measure FORCs to more finely interpret the grain size mixtures/domain states in a sample. FORC diagrams are smoothed using the locally weighted regression smoothing (LOESS) technique and the FORCinel 3.08 program (Harrison and Feinberg, 2008), with this process completed to reduce noise in the generated FORC. As interpreting FORCs can be somewhat complex, we refer the reader to Bilardello and Egli in IRM Quarterlies 30-4 and 31-2 for a summation of research on FORC interpretation.

(1) $HIRM = 0.5 \times (SIRM + IRM_{-0.3\,T})$

(2) $S\text{-ratio} = (1 - (IRM_{-0.3\,T} / SIRM_{1\,T})) / 2$

3.1.2. Low Temperature Experiments

Field-cooled (FC), zero-field cooled (ZFC), low temperature saturation isothermal remanent magnetization (LTSIRM), and room temperature saturation isothermal remanent magnetization (RTSIRM) sequences were conducted on the Magnetic Properties Measurement System (MPMS) 3. Broadly, these experiments involve cooling the specimen to low temperature (10 K), and raising it back up to room temperature with a field (2.5 T) either on or off at specific moments to produce a remanence. For a more detailed explanation of these experiments, see Bilardello and Jackson in IRM Quarterly 23-3. These experiments were used to identify magnetic mineralogy, the presence of oxidation, and the domain state (grain size) of magnetite within a specimen.

Alternating current (AC) measurements were also completed on the MPMS 3, but for only 6 representative specimens. This experiment measured the susceptibility of the specimens at three frequencies (1, 10, and 100 Hz) on warming from low temperature to room temperature. AC measurements were primarily used to check for the presence of superparamagnetic and/or paramagnetic grain populations, with our specimens exhibiting both types of grains (section 4.1.1.). Superparamagnetic (SP) grains are very small and their magnetization constantly flips at room temperature, and while they can acquire a magnetization under an applied field, they will immediately lose it once the applied field has been removed. Paramagnetic grains have no magnetization at room temperature, but like SP grains will gain a temporary magnetization under an applied field that will be lost once the field is turned off. We test for SP grains in particular as they can influence hysteresis loops, the parameters of which can be used to assess domain state in the Day plot (Day et al., 1977).

3.2. Archaeomagnetic Methods

Archaeointensities were determined using thermal experiments. For this experiment only the intensity of the ancient magnetic field was of interest, as none of our sherds were discovered in the orientations in which they were originally fired. Pseudo-Thellier experiments were also completed, but as they were largely unsuccessful they have been omitted from this thesis. All archaeointensity experiments were performed within the IRM's shielded room.

3.2.1. Thermal Archaeointensity Experiment

Specimens were heated within an ASC Model TD-48SC Thermal Specimen Demagnetizer with inbuilt cooling fan. A BK Precision DC Power Supply was used to generate fields within the oven. To complete a thermal archaeointensity experiment, we followed the IZZI protocol outlined by Tauxe and Staudigel (2004), based on the Thellier and Thellier (1959) protocol. Specimens were heated in coarse steps of 50 degrees from 100°C to 300°C, and then in finer steps of 25 degrees from 300°C to 575°C, with the final zero field, infield, infield, zero field (ZI, IZ) couplets completed in even finer steps moving from 575°C to 585°C, until a maximum temperature of 600°C. pTRM checks (Thellier and Thellier, 1959) started after 200°C, and followed every two couplets. For each temperature step, the specimens were held at temperature for 30 minutes, then cooled with the oven fan on for 60 minutes, after which the remanence of the specimen was measured on the 2G. For infield steps the field was applied during both heating and cooling steps. However, for 15 specimens the field was only applied during cooling for infield steps at 100°C, 150°C, and 200°C. This was an oversight, and after this

deviation was noticed the experiment was continued with the field on during the entirety for the remaining infield steps.

The result of this experiment is the Arai plot, which compares the NRM remaining in the sample after each temperature step with the pTRM gained by the sample at that same temperature step under our applied lab field (40 μT). The slope of this line, created using the stepwise removal and acquisition of remanence, can be plugged into Equation 3 along with the applied lab field to generate the ancient field intensity (archaeointensity) that acted on the sample when it was fired. Equation 3 is based on the linear relationship between the applied magnetic field and the acquisition of pTRM, and is assumed to be true for single domain (SD) and, potentially, vortex grains. Ceramic sherds can sometimes record the geomagnetic field of multiple heating events, with an initial high temperature firing event associated with the vessel's creation and a later low temperature heating event related to the use of the vessel as a cooking pot. We refer to the higher temperature creation of the vessel as the primary component of magnetization, and the later low temperature reheating of the vessel as the secondary component of magnetization.

Vector endpoint diagrams plot the directional and intensity components of a sample's magnetization on a 2D coordinate system, making it easier to separate different magnetic recordings. Selection criteria are implemented as a quality control for Arai plots, ensuring only trustworthy slopes are used, though they are not a replacement for manual inspection of the plots. We assessed our IZZI experiment using a modified version of the SELCRIT2 criteria (Biggin et al., 2007; Paterson et al., 2014). Slopes were only used to calculate an archaeointensity if they passed this selection criteria (or only failed 1 criterion) and appeared to be representative of the

primary or secondary component based on the vector endpoint diagram (Zijderveld, 2013). A table of the criterion values used for modified SELCRIT2 can be found in Table 2. For descriptions of these modified criterions we refer the reader to the Standard Paleointensity Definitions v1.2.0 document (Paterson et al., 2014). Archaeointensities were calculated using the Thellier GUI application (Tauxe et al., 2016).

(3) $B_{anc} = (M_{NRM} / M_{lab}) * B_{lab}$

3.2.2. Magnetic Anisotropy Correction

When a ceramic vessel is molded the method of manufacture can impart a preferred orientation to its magnetic grains, causing anisotropy to occur. In Minnesota, the majority of ceramics are coil spun, so cigar shaped (prolate) grains may have been re-oriented by the creator of the vessel through the process of rolling clay coils. As the acquisition of intensity can be affected if the lab field is not applied in the exact same orientation as during the original firing, different degrees of anisotropy can impact the magnitude of our calculated archaeointensity, necessitating a correction for this effect. Thermal anisotropy correction experiments were conducted with this in mind, and followed the method of Shaar et al. (2016). Specimens were subjected to the highest temperature reached during the thermal experiment (600°C) by orienting the specimens in the oven in six positions (+x, +y, +z, -x, -y, -z), one position for each heating and measuring step. Specimens were heated under an applied DC field of 40 μT, with a baseline measurement (subtracted from the infield measurements) conducted at this same temperature in zero field at the beginning of the experiment. Additionally, the +x orientation was repeated at the

end of the experiment as an alteration check. After each step the TRM of the specimen was measured on the 2G.

The influence of anisotropy was determined by calculation of the relative percent difference between the three pairs of orientations [(+x, -x), (+y, -y), (+z, -z)], and the initial and final +x orientation alteration checks. If the difference was greater than 5% for any pair (Aitken et al., 1981), we rejected the anisotropy of thermoremanent magnetization (ATRM) results and conducted an anisotropy of anhysteretic remanent magnetization (AARM) correction experiment. AARM experiments were conducted by demagnetizing the specimens at 170 mT and measuring the NRM as a baseline on the 2G, followed by the application of an ARM under a DC bias field of 40 μT on the DTech, and the subsequent measurement of the imparted ARM on the 2G. This method was repeated for 6 orientations (+x, +y, +z, -x, -y, -z), and is very similar to an ATRM correction experiment, but requires a baseline step prior to every orientation rather than just at the beginning of the experiment (Tauxe, 2018). Additionally, AARM experiments don't require an alteration check at the end, as they use alternating magnetic fields instead of thermal energy, which does not cause mineral alteration in a specimen.

AARM experiments needed to be completed instead of ATRM for 5 samples (1350-7B, 881-1B, 881-1C, 573-6, and 1135), with only sample 1179 excluded from the correction experiments entirely. AARM experiments used a new fragment for each sample which hadn't been subjected to any thermal methods. However, we could not complete an AARM experiment for sample 1135, as the fragments were too irregularly shaped to properly orient. All 4 remaining samples showed relative percent differences for each pair of orientations below 5%, however, AARM experiments were only successful for 3 of the 4, as sample 881-1B reported an inflated

anisotropy correction factor (8.28) for our chosen temperature interval. Therefore, for this specimen we will only use the cooling rate corrected intensity (as with sample 1135), as it will be closer to the true intensity than that given by the inflated anisotropy correction factor. Anisotropy tensors for ATRMs and AARMs were calculated using Thellier GUI (Tauxe et al., 2016). Anisotropy correction factors are in Table 4, F-test (Hext, 1963) results are reported in Table 5. Of the eighteen specimens we performed anisotropy corrections on, seven had F-test values that exceeded the critical F-value (3.1059). Generally, thinner sherds (around 4 mm) appeared to have the highest and lowest (or most variable) anisotropy corrections (Figure 3).

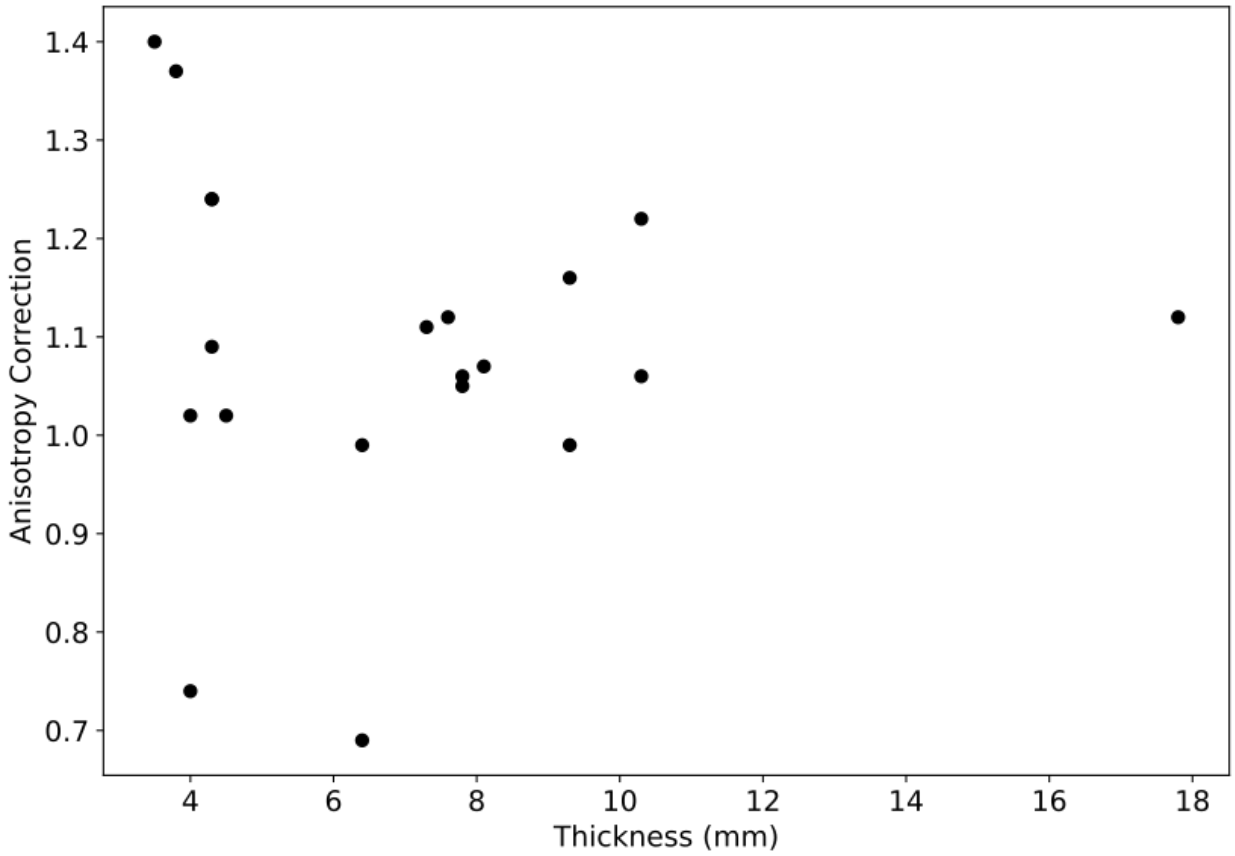

Figure 3. Anisotropy correction factor plotted against sample thickness. Minimum and maximum correction factors occur at lower thicknesses, showing greater variability for thinner sherds. The inflated anisotropy correction factor (8.28) of specimen 881-1B has been omitted from this plot.

3.2.3. Cooling Rate Correction

Cooling rate experiments aim to correct the thermal experiment so that the acquisition of remanence better mimics the conditions under which our ceramics were fired. In the lab, cooling specimens with an oven fan is much faster than in a fire pit or kiln, where vessels would cool slowly over the course of a day (or longer). This discrepancy between lab and actual cooling rates can impact the magnitude of the TRM recorded, with slower cooling rates typically resulting in higher intensities in pottery dominated by SD magnetite or hematite (Halgedahl et al., 1980).

To measure the impact of cooling rate on our acquired TRMs, we followed the methodology described in Shaar et al. (2016), a procedure similar to that of Chauvin et al. (2000) and Genevey and Gallet (2002). For this method, specimens are demagnetized in zero field at 600°C as a baseline step, followed by a fast (60 minute) infield step (FastInitial), a slow (24 hour) infield step (Slow), and then another fast infield step as an alteration check (FastFinal). All steps were completed at 600°C and in a 40 μT field. Cooling rates were rejected if alteration was greater than 5%, gauged by the percent difference between the fast infield step pairs. All specimens (excluding sample 1179, which was not tested) had passing alteration checks. The cooling rate correction (CRC) is defined as the ratio between the average of the fast cooling rates over the slow cooling rate, given by Equation 4. Cooling rate correction factors are in Table 4.

(4) $CRC = ((Fast_{Initial} + Fast_{Final}) / 2) / Slow$

3.3. Electron Microscopy

Scanning electron microscopy (SEM) and energy dispersive spectroscopy (EDS) analysis was conducted on 6 representative specimens at the UMN CharFac using a Thermo Fisher Scientific Apreo 2S Lo-Vac SEM with Oxford Instruments Ultimax 100 mm^2 and AZtec Live chemical imaging EDS. Some specimens were analyzed in lo-vac mode without a carbon coating (providing lower resolution), but most were carbon coated for hi-vac analysis. We note that the SEM only allows us to analyze larger particles and cannot show particles at the nanometer scale, so SD particles cannot be identified through this method. However, vortex and multi-domain (MD) grains may be visible, though they may not be the grains carrying the primary remanence. SEM-EDS analysis was completed primarily to identify common magnetic minerals in the specimens, and to investigate visible oxidation rinds.

4. Results and Discussion

4.1. Rock Magnetic Results

We plotted total magnetic susceptibility as box and whisker plots to ascertain the variability of susceptibility between specimens for a given sample (Figure 4). Each sample (e.g. sample 1325) was split up into 4 specimens (e.g. 1325-01, 1325-02, 1325-03, and 1325-04). The majority of samples showed minimal variability in susceptibility between specimens, with the exception of samples 1220, 1350-7B, and 988, which showed the greatest spread in our collection. Additionally, samples 1220, 441, and 573-6 had a specimen with an outlying susceptibility. Sample 1220 in particular had both the largest spread of susceptibilities and the largest outlier. Though, with the exception of sample 1220, the bulk of our samples appear to have internal homogeneity between specimens. Mean susceptibilities ranged from the 10-7 to 10-5 orders of magnitude for our samples (Table 3).

AF demagnetization of the sherds yielded broadly similar plots, with the exception of sample 1179, which appeared more multi-domain (MD) in character at low AF steps, and sample 1350-4B, which had a higher median destructive field (MDF) than the other specimens. For our samples, average MDF values were around 27 mT, with the lowest and highest MDFs reported 16 mT and 64 mT respectively (Table 3). High MDFs indicate a specimen is more likely to remain stable against alternating fields, and therefore be more able to retain a magnetic field recording over long periods of time without being demagnetized, a necessary quality of strong archaeointensity recorders.

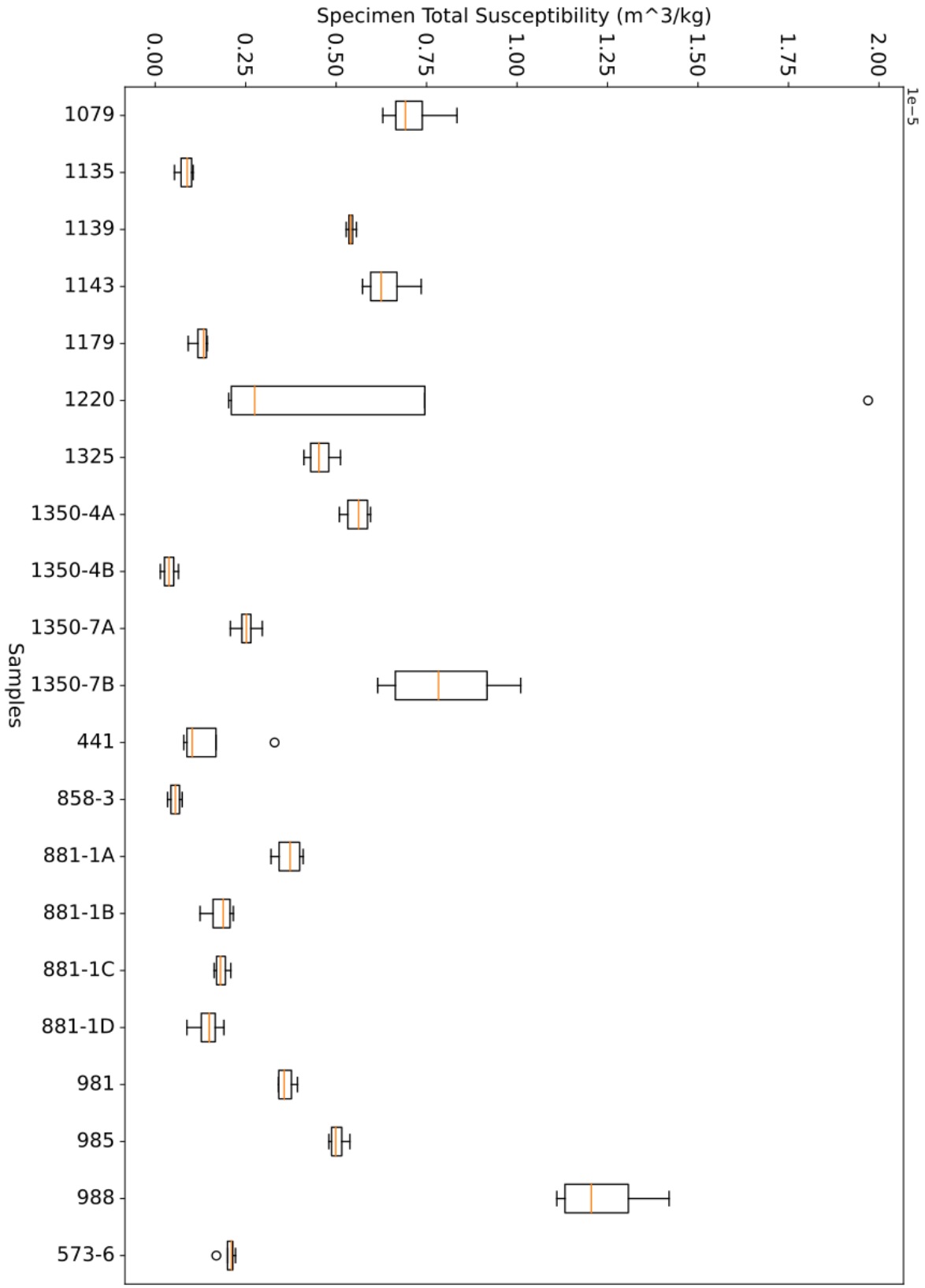
Specimen Total Susceptibility (m^3/kg)
0.00
0.25
0.50
0.75
1.00
1.25
1.50
1.75
2.00
1e−5
Samples
1079
1135
1139
1143
1179
1220
1325
1350-4A
1350-4B
1350-7A
1350-7B
441
858-3
881-1A
881-1B
881-1C
881-1D
981
985
988
573-6

Figure 4. Box and whisker showing the variation in susceptibility for a sample between its 4 specimens. A sample (e.g. 1179) is cut into four specimens (e.g. 1179-01, 1179-02, 1179-03, 1179-03) so that it can be used for multiple types of analysis. The purpose of this box and whisker plot is to see if the specimens are internally homogeneous, which appears to be the case for the majority of specimens, with the exception of 1220.

4.1.1. Magnetic Grain Size and Domain States

The Day plot (Day et al., 1977) can be used to identify domain states, and compares two bulk hysteresis parameter ratios: remanent coercive force (Bcr) over coercive force (Bc) on the x-axis, and saturation remanent magnetization (Mr) over saturation magnetization (Ms) on the y-axis (Table 3). The Day plot is divided into regions corresponding to SD, vortex or SD/MD mixtures, and MD grains. Notably, the mixing curves and ratio thresholds on the Day plot were designed explicitly for magnetite, as it is not yet certain in the field how the ratios of other minerals would plot. So, mixtures of minerals may influence where ratios are plotted, and the plot can be further complicated by a variety of other factors that can enhance or suppress Mr/Ms and Bcr/Bc ratios (see Tauxe, 2018). Regardless, the Day plot is a useful first pass for determining domain state, and some of the factors that can influence Day plot ratios (like grain size mixtures and particle interactions) can be assessed using FORC diagrams (Roberts et al., 2000).

Using the modified MD and SD limits of Dunlop (2002a), 16 specimens were categorized as vortex or SD/MD mixtures, and 1 as MD (sample 1179), with 4 plotting to the right of the vortex (or SD/MD mixture) boundary (Figure 5). The one sherd that failed all aspects of the

archaeointensity experiment (sample 1179; F-tier) fell within the MD section of the plot, otherwise, there was no clear distinction between thermal quality tiers visible on the Day plot (see section 4.2. for an explanation of thermal quality tiers). Additionally, rim sherds seemed to have a more variable distribution on the Day plot compared to body sherds, and were the only types of sherd that plotted to the right of the vortex or SD/MD mixture boundary. Specimens that plotted to the right of the vortex or SD/MD mixture boundary can potentially be explained by contributions of fine SP particles (Pick and Tauxe, 1994), or through multi-mineral mixtures (e.g., maghemite and hematite), which can shift the Bcr/Bc ratio outside the typical Day plot boxes. To determine which type of grain size mixture is occurring, we used the sigma value parameter (Fabian, 2003) to quantify hysteresis loop shape. Specifically, we are interested in whether the loop is “wasp-waisted,” with a constricted middle and a positive sigma, or “pot-bellied” (Tauxe et al., 1996), with a widened center and negative sigma.

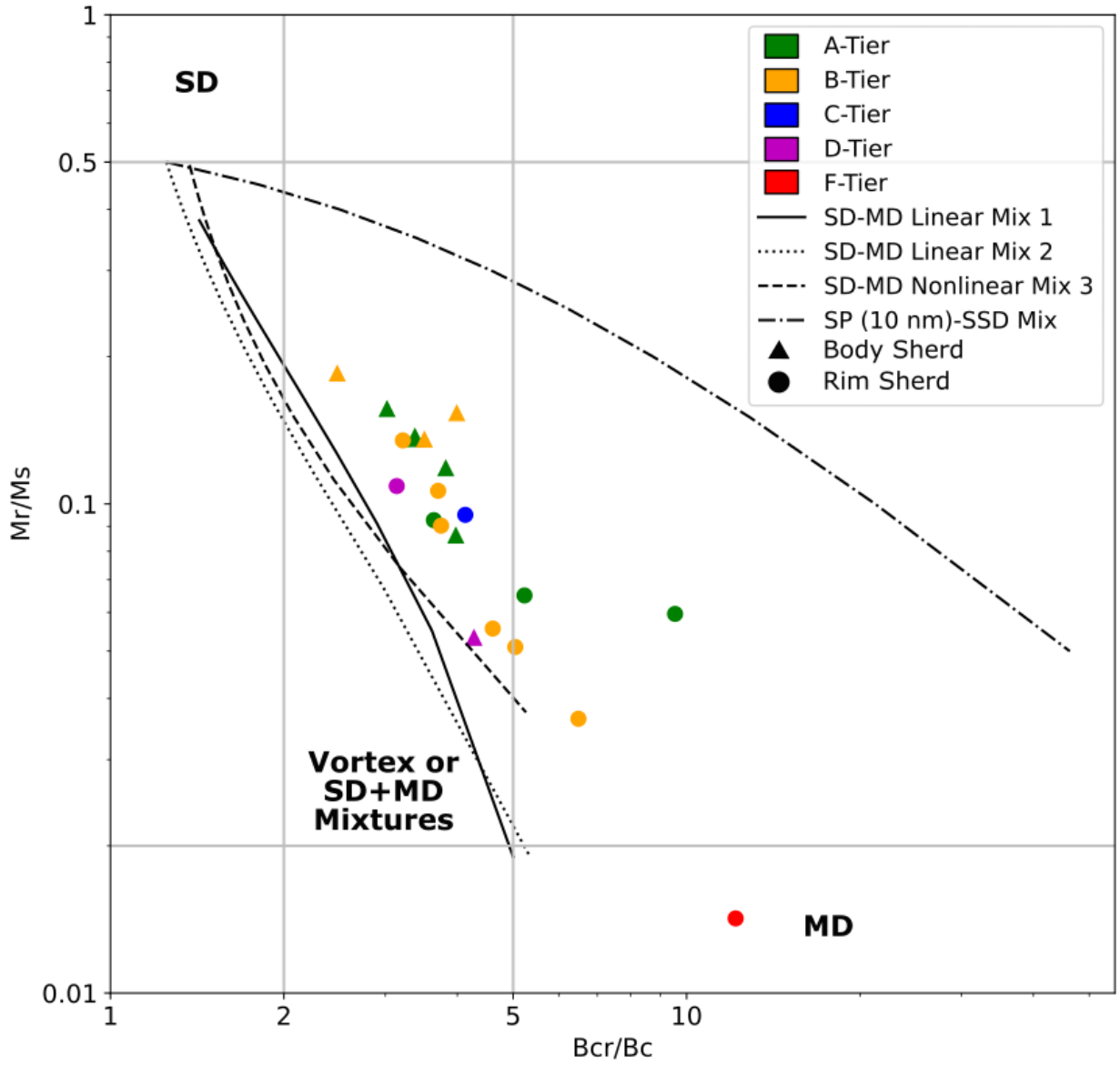

Figure 5. Logarithmic Day plot of sherds. SD refers to single domain and MD multi-domain. Rim and body sherds are distinguished by circles and triangles, with color denoting the quality tier of the sherd ranging from A (pass all selection criteria) to F (fail all aspects of the archaeointensity experiment). Quality tiers are explained in section 4.2. Sherds in A, B, and C tiers are considered promising for the creation of an archaeomagnetic reference curve. Dunlop (2002a)'s SD-MD mixing curves are distinguished by different line styles.

Eighteen of our specimens had negative sigma values, leaving 3 characterized as wasp-waisted (Table 3). Of the 3 specimens exhibiting wasp-waisted loops, only sample 1135 (Figure 6a) was among those that also plotted to the right of the vortex or SD/MD mixture boundary, with this specimen also having the highest magnitude sigma value reported (0.38). Additionally, sample 1135 demonstrated a second higher coercivity peak in the derivative of saturation remanence (Mr) as a function of applied field on a logarithmic axis plot (coercivity distribution; Figure 6b) that could explain the wasp-waisted distortion of the loop (distinct hematite and magnetite populations, see section 4.1.2.). The 18 specimens with pot-bellied loops may have contributions of small SP particles that are distorting their loops (Tauxe et al., 1996).

SP populations can be confirmed using AC experiments of susceptibility measured with temperature, with frequency dependence (Equation 5) an indication of SP populations, as SP grains can switch to SD grains at high frequencies (Thompson and Oldfield, 1986). Susceptibility measurements at low temperature were completed on 6 representative specimens, all of which demonstrated the presence of potential SP populations, with the exception of sample 1179, which showed a much more restricted frequency dependence than the other 5 specimens (Figure 7). Additionally, 3 specimens (left column of Figure 7) displayed steep slopes at low temperature, suggesting paramagnetic components.

(5) $FD = ((X'(1.0\ Hz) - X'(100.1\ Hz)) / (X'(1.0\ Hz))) * 100$

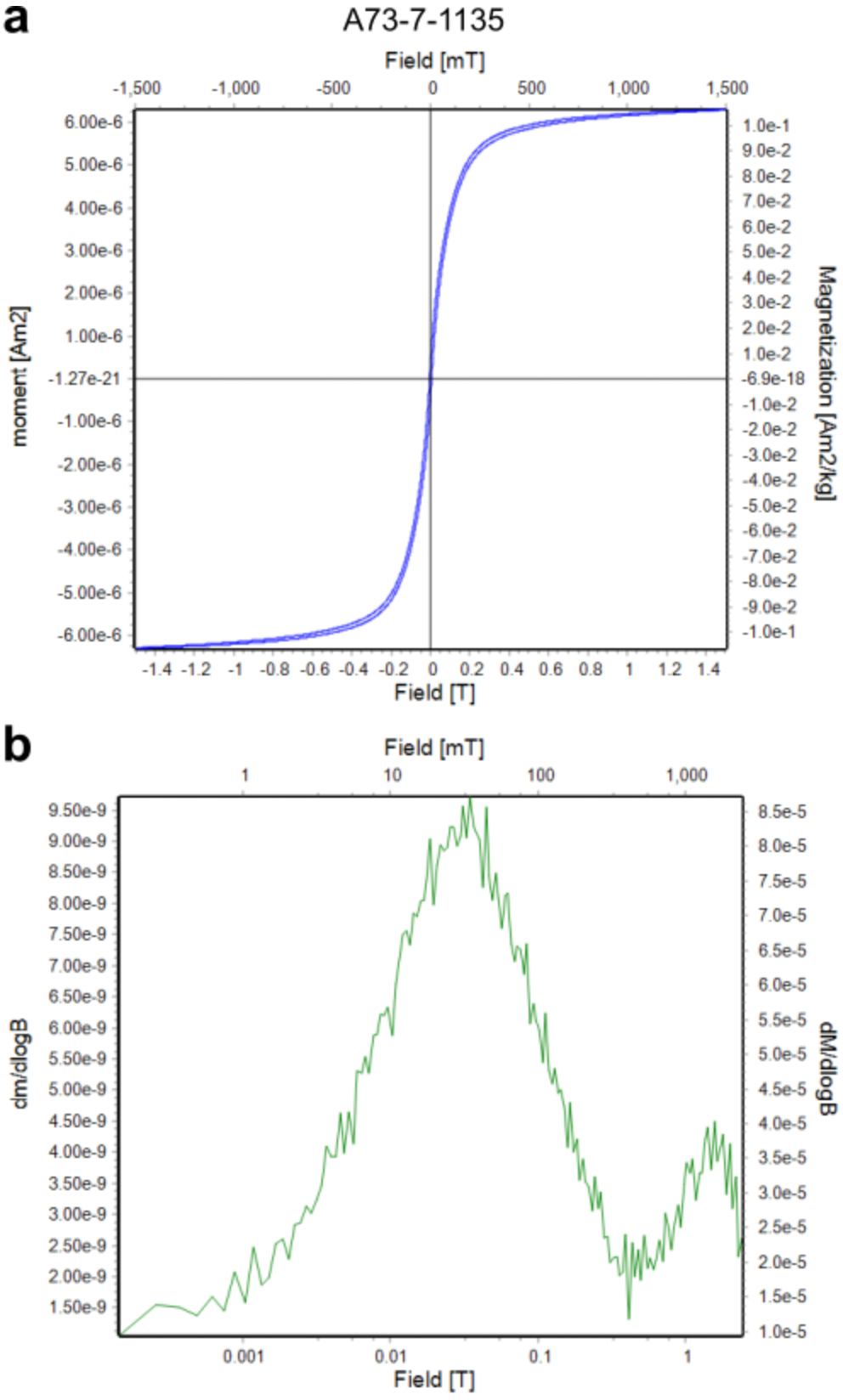
a
A73-7-1135
Field [mT]
-1,500
-1,000
-500
0
500
1,000
1,500
6.00e-6
5.00e-6
4.00e-6
3.00e-6
2.00e-6
1.00e-6
-1.27e-21
-1.00e-6
-2.00e-6
-3.00e-6
-4.00e-6
-5.00e-6
-6.00e-6
moment [Am2]
1.0e-1
9.0e-2
8.0e-2
7.0e-2
6.0e-2
5.0e-2
4.0e-2
3.0e-2
2.0e-2
1.0e-2
-6.9e-18
-1.0e-2
-2.0e-2
-3.0e-2
-4.0e-2
-5.0e-2
-6.0e-2
-7.0e-2
-8.0e-2
-9.0e-2
-1.0e-1
Magnetization [Am2/kg]
-1.4 -1.2 -1 -0.8 -0.6 -0.4 -0.2 0 0.2 0.4 0.6 0.8 1 1.2 1.4
Field [T]
b
Field [mT]
1
10
100
1,000
9.50e-9
9.00e-9
8.50e-9
8.00e-9
7.50e-9
7.00e-9
6.50e-9
6.00e-9
5.50e-9
5.00e-9
4.50e-9
4.00e-9
3.50e-9
3.00e-9
2.50e-9
2.00e-9
1.50e-9
dm/dlogB
8.5e-5
8.0e-5
7.5e-5
7.0e-5
6.5e-5
6.0e-5
5.5e-5
5.0e-5
4.5e-5
4.0e-5
3.5e-5
3.0e-5
2.5e-5
2.0e-5
1.5e-5
1.0e-5
dM/dlogB
0.001
0.01
0.1
1
Field [T]

Figure 6. Hysteresis loop and coercivity distribution for sample 1135. (a) Hysteresis loop is wasp-waisted and slope corrected. (b) Coercivity distribution shows the cause of the wasp-waisting, a mixture of two discrete coercivity populations, likely magnetite and hematite.

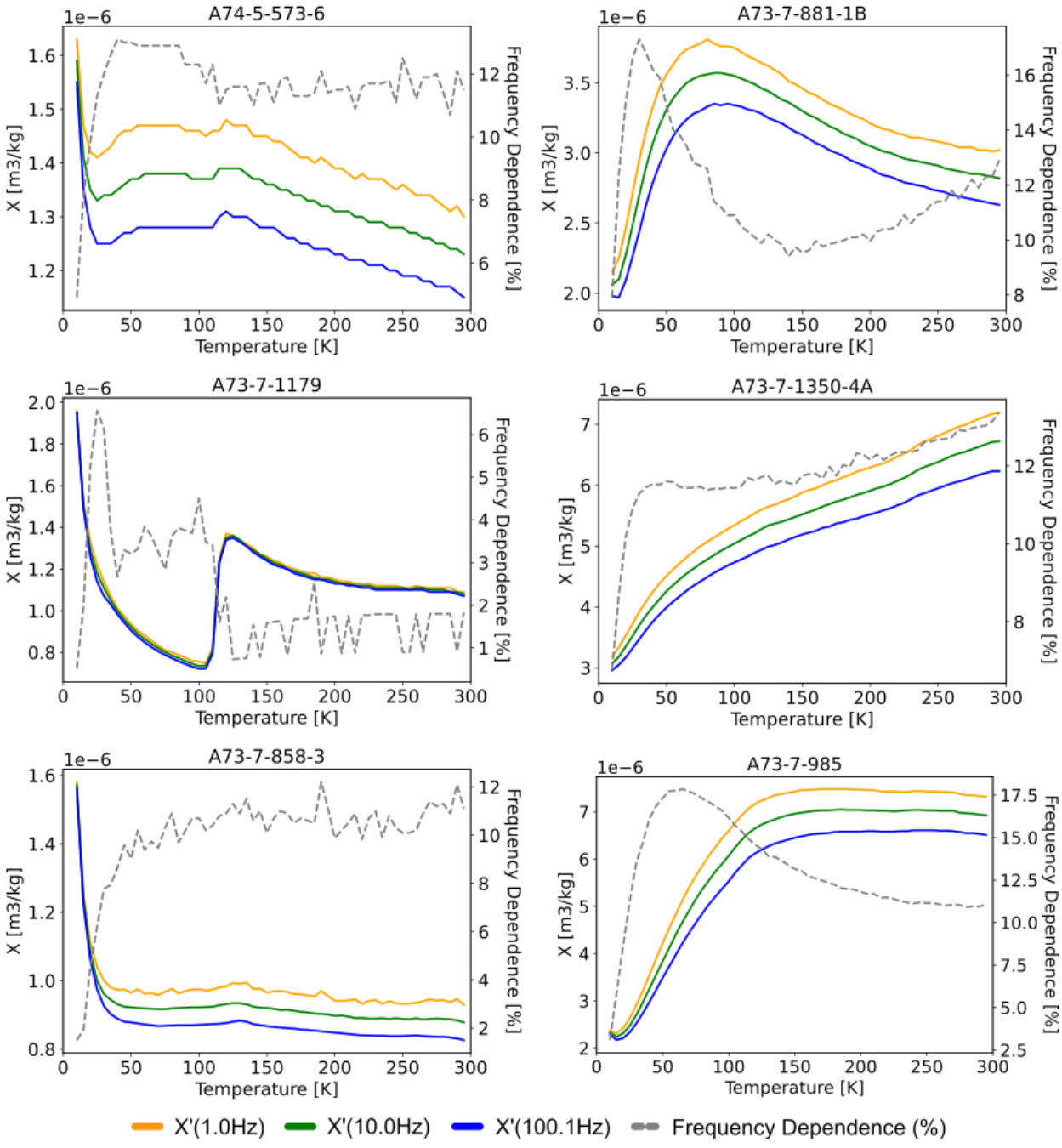

Figure 7. Variation of mass normalized susceptibility measured at 3 AC frequencies (1, 10, and 100 Hz) on warming from low temperature (10 K) to room temperature (300 K) for six representative specimens. Frequency dependence is shown as a dashed gray line.

The distribution of magnetization in a specimen, inferred to relate to domain state and interaction fields, can be visualized through FORC diagrams. We interpret our specimen's FORC diagrams as showing variable mixtures of vortex and MD grains (Figure 8a) in most specimens, except for sample 1179 (Figure 8b), which appeared to be primarily MD. Additionally, our specimens all showed tails along the central ridge (Bu = 0) extending towards high coercivities, indicating minor contributions of fine SD particles within each specimen. Samples 441 and 1135 plotted to the right of the vortex (or SD/MD mixture) Day plot boundary (with Bcr/Bc ratios > 6), and demonstrated higher proportions of MD grains than the other specimens (Figures 8c and 8d). These domain states were also broadly supported by our low temperature experiments, with only sample 1179 appearing MD on the FC-ZFC plot. Our specimens also all demonstrated minimal magnetostatic interactions and vortex spreading, which we quantified using full width at half maximum (FWHM; see Carvallo et al., 2006) values. Carvallo et al. (2006) suggests a FWHM paleointensity rejection threshold of 29 mT and above, with our samples showing FWHM values on the Bc = 0 axis between 2 and 17 mT (Table 3).

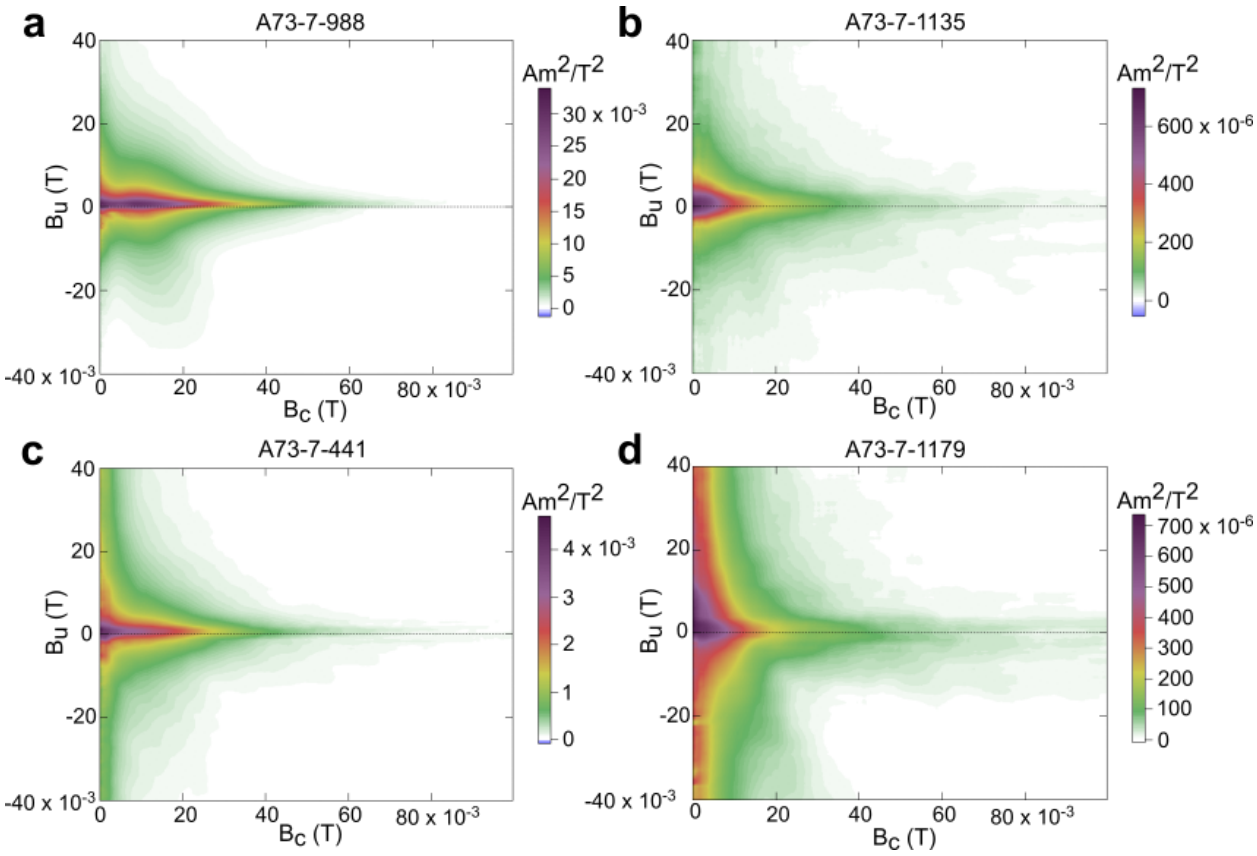

Figure 8. Representative FORC diagrams, interpreted to be a mixture of vortex state and MD grains, with variations in (a) through (d) showing increasing MD contributions.

4.1.2. Magnetic Mineralogy

The presence of common magnetic minerals like magnetite, maghemite, titanomagnetite, hematite, and goethite are confirmed (or suggested) using low temperature experiments. Sixteen of our specimens displayed a visible Verwey transition (appearing around 120 K) in either one or both of our low temperature experiments, indicating that magnetite is present (Figure 9). For the 5 specimens missing the Verwey transition, it is possible they are more predominantly composed of titanomagnetite, if there has been Ti-substitution, or maghemite, if oxidation has occurred.

Two of these specimens show evidence of maghemite in the RTSIRM curves, with the other 3 having RTSIRM curves suggestive of goethite (samples 881-1B, 881-1C, and 881-1D in Figure 10). Maghemite can be identified in a specimen using the “humpiness” of RTSIRM curves (Özdemir and Dunlop, 2010). Based on this observation, 14 specimens showed plots sufficiently “humpy” to suggest evidence for the partial oxidation of magnetite (Figure 9b/9d). We see evidence for goethite in the separation of FC-ZFC curves up to room temperature (true for all samples except 1179) and in negatively sloping RTSIRM curves, typically resembling parabolas (true for 6 specimens; Figure 10).

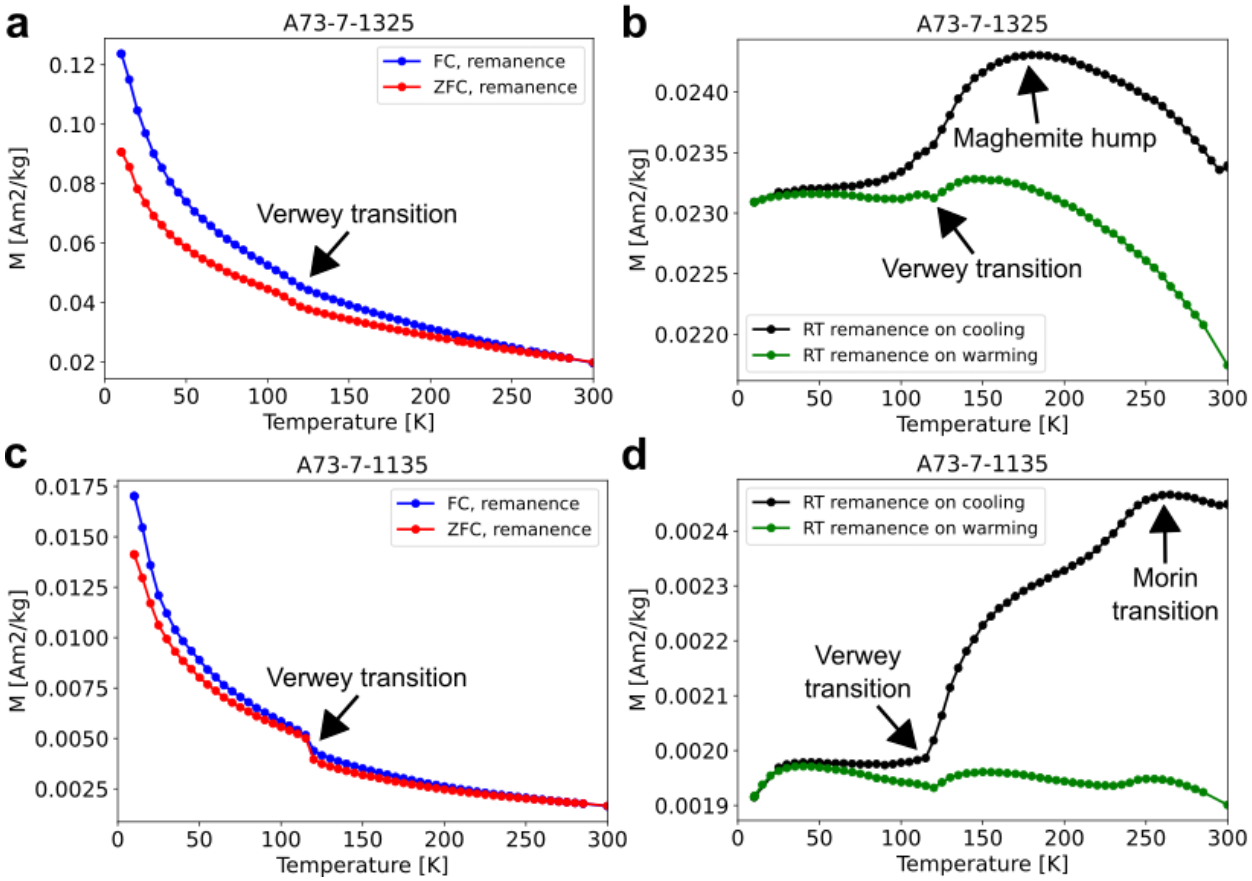

Figure 9. Representative low temperature experiments. Significant transitions are highlighted with arrows (Verwey and Morin). Most specimens show a Verwey transition more similar to (a) than (c). (a) and (c) show FC-ZFC plots, with (b) and (d) showing RTSIRM experiments.

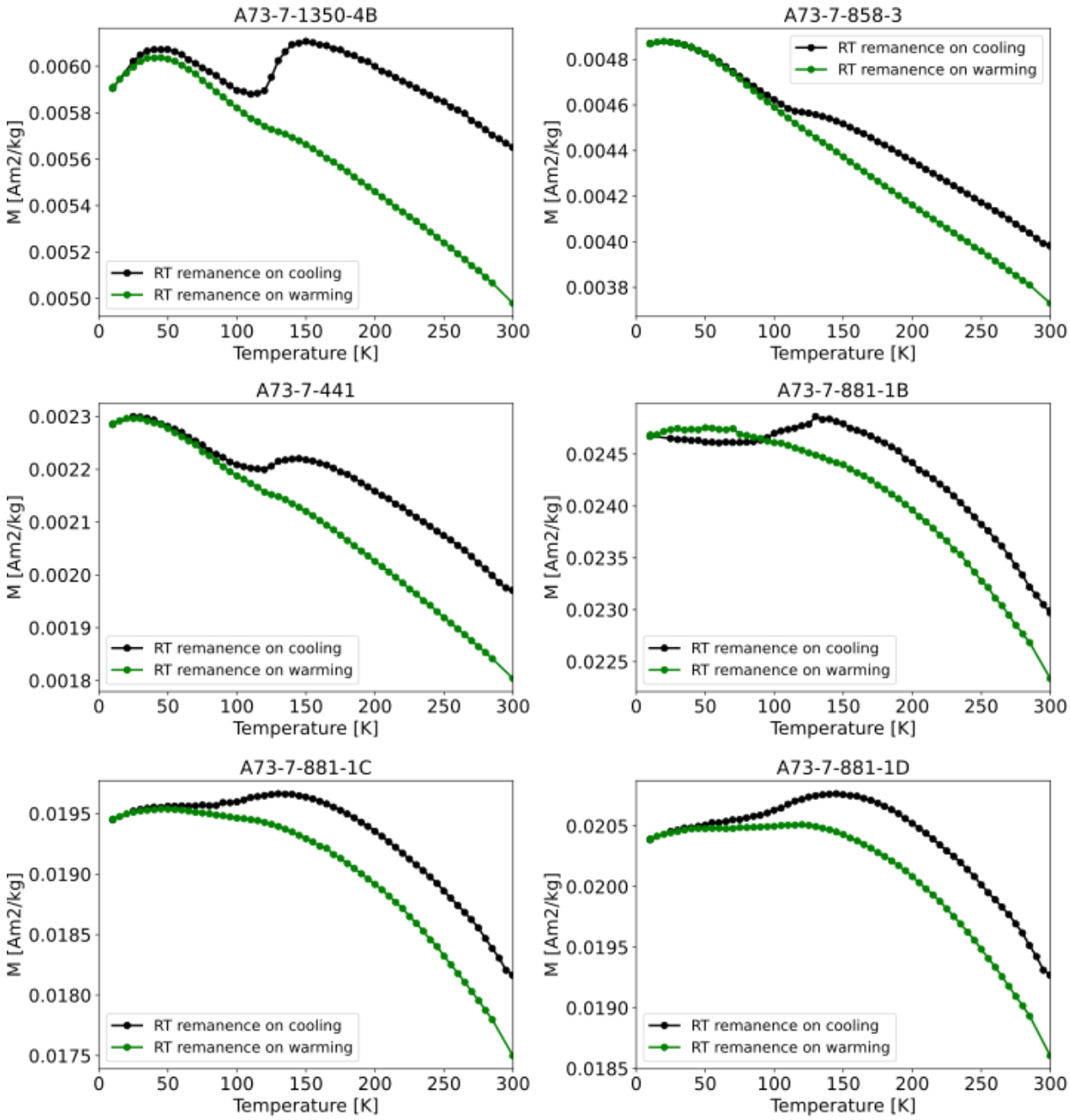

Figure 10. RTSIRM plots suggestive of goethite with partially oxidized magnetite (maghemite) or titanomagnetite.

If our specimens have a hematite component it may appear as the Morin transition at around 250-260 K in one or both low temperature plots, though this transition will not necessarily appear if magnetite is present (as for our samples). Only sample 1135 showed a clear Morin transition in the RTSIRM plot (Figure 9d), with sample 1350-4B showing only a slight Morin transition, indicating significant populations of hematite in both. Additionally, sample 1135 exhibited a secondary high coercivity peak in the coercivity distribution, which can be attributed to hematite (Figure 6b). All other specimens showed a singular low coercivity peak in this plot, attributed to magnetite/maghemite. HIRM values (Table 3) indicated very minor hematite/goethite concentrations in all specimens, however, through other analyses some specimens have shown evidence for large concentrations of hematite, as well as goethite. While these high coercivity minerals are present in the sample, the HIRM values indicate that they are likely not large contributors to the total remanence. S-ratios were all approaching unity, indicating the dominance of low coercivity minerals like magnetite/maghemite in all specimens. Only samples 1135 and 1350-4B had S-ratios below 0.90 (Table 3), with these also the only specimens showing evidence for hematite. Primary low coercivity mineral populations are also supported by our FORC diagrams, all of which had primary signal peaks at low coercivities (Figure 8).

The Arai plots from our thermal procedure can further validate these conclusions. For most specimens the majority of remanence was removed by 600°C, a characteristic of magnetite. In the case of the exceptions, sample 1179 lacks a stable remanence, while sample 1135 (Figure 11) had an increase in remanence after 400°C, and was not fully demagnetized by 585°C. Three other specimens (samples 881-1B, 881-1C, and 881-1D; Figure 11) displayed similar behavior to sample 1135, but were fully demagnetized by 600°C. The secondary components of these four

specimens are potentially the result of reheating events that overprinted the original remanence, with the remaining remanence in sample 1135 attributed to the sherds high coercivity hematite contribution.

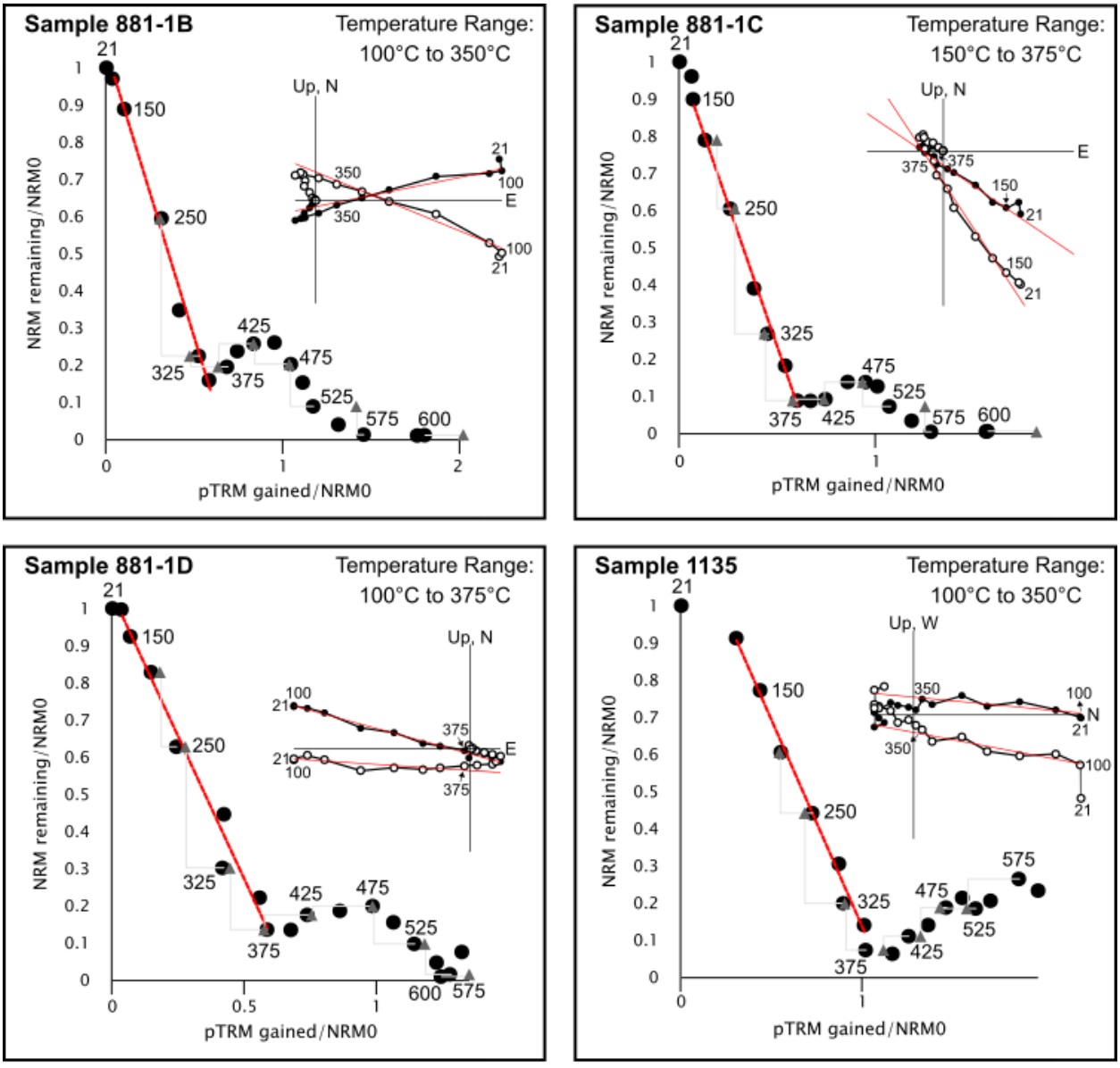

Figure 11. Arai plots and vector endpoint diagrams for sherds with potential overprints. The dashed red line shows the temperature interval chosen for the selected component. Gray triangles

show pTRM checks. An instrumental error at 200°C was removed from the plot for sample 881-1B. Samples 881-1B, 881-1C, and 881-1D were found at the same depth level at the same site, but are thought to be from separate vessels. All four specimens show an increase in remanence after 400°C manifesting as a hump in the Arai plot, with specimens 881-1B, 881-1C, and 881-1D fully demagnetizing by 600°C. In contrast, specimen 1135 still has a substantial amount of remanence left after this temperature.

Of the 6 sherds subjected to SEM-EDS analysis, samples 985, 858-3, and 573-6 had visible iron titanium oxides (confirmed through EDS), with sample 985 featuring magnetite, and both samples 985 and 573-6 showing titanomagnetite. Additionally, the ratio of calcium to oxygen in a large shell fragment in sample 858-3 is characteristic of an oxygen poor environment (Figure 12b), indicating the vessel may have been smudged or smothered (fired in an oxygen reducing environment). We also analyzed the elemental concentration of the oxidation rind in sample 573-6, and found that iron concentration was constant within the rind and interior of the sherd. This suggests the iron was not mobile during firing, and that subsequent use and exposure to groundwater did not create secondary Fe-mineralization (Figure 12a).

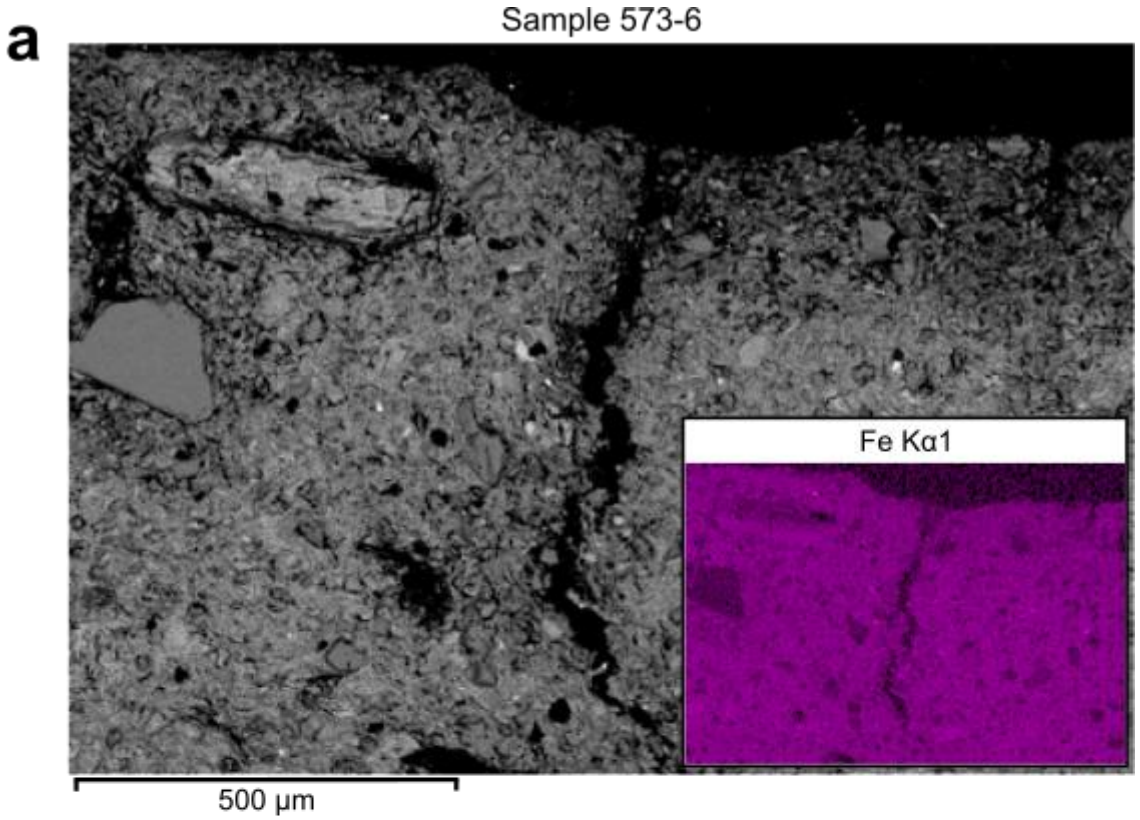
a
Sample 573-6
Fe Kα1
500 µm

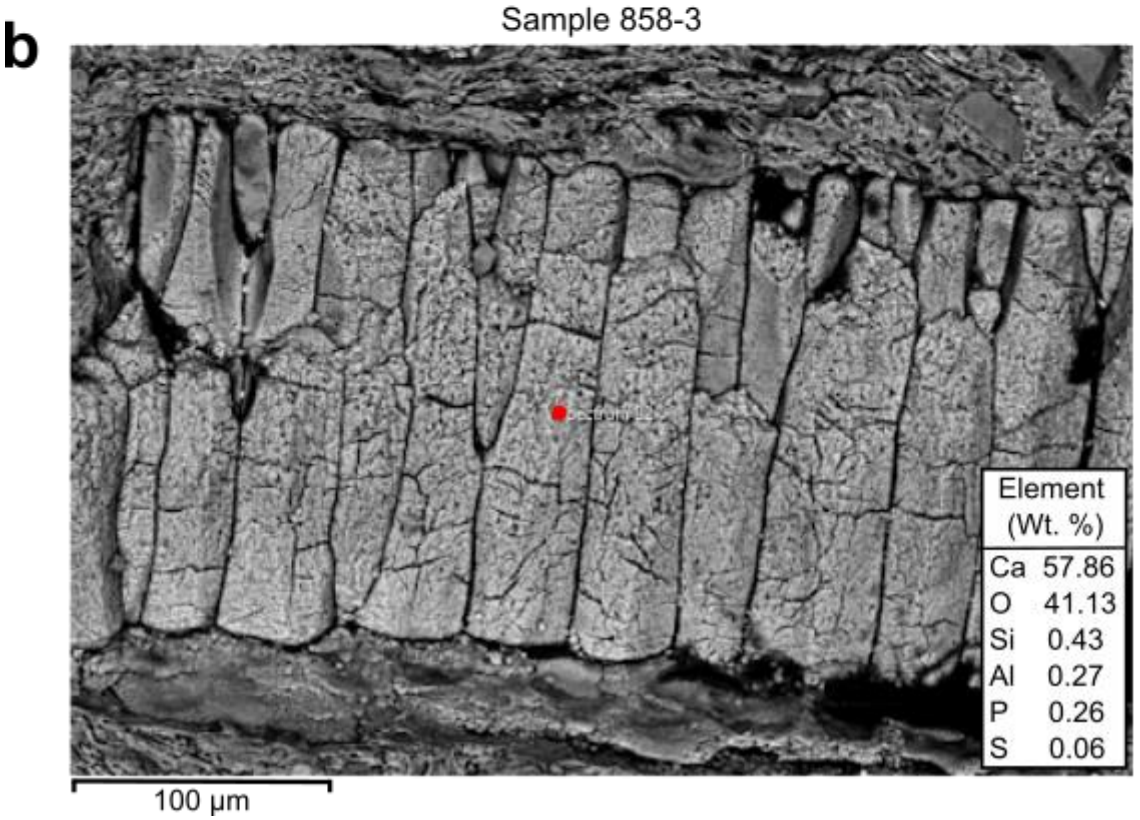
b
Sample 858-3
Element (Wt. %)
Ca 57.86
O 41.13
Si 0.43
Al 0.27
P 0.26
S 0.06
100 µm

Figure 12. Selected electron microscopy images. (a) Backscattered electron image with an inset showing elemental concentration of iron in the oxidation rind of sample 573-6. (b) Backscattered electron image of shell temper in sample 858-3. Spectrum data point (in red) showing the measurement location for elemental data reported in inset. Measurement was taken near the center of the shell to minimize potential contamination from the surrounding ceramic matrix.

4.2. Archaeointensities and Sherd Quality

Selection criteria are a useful tool to assess the robustness of Arai plots, and can quantify how well a sample magnetically behaves for the purposes of archaeointensity experiments. However, while these criteria are useful they do not provide the final say and are more akin to guidelines. So, failing a particular criterion does not necessarily mean a sample is not usable for an ARC. Therefore, to best show the promise of Minnesota ceramics as a medium, we categorize sherds in quality tiers based on one of the "looser" selection criterias, modified SELCRIT2. For this study, "A-tier" sherds are those that have either a primary and/or secondary component that passed modified SELCRIT2, while "B-tier" sherds are those that show promising behavior but fail one criterion of modified SELCRIT2 for a component, and/or show minor visual curvature in the Arai plot (Figure 13). We also added a C-tier for one particularly curved specimen with a component that passed SELCRIT2. We did not attempt to calculate archaeointensities for three specimens, two of which did not have a fit that failed less than 2 criterions (D-tier), with sample 1179 the only sherd that produced a noisy Arai plot without any interpretable components (F-tier).

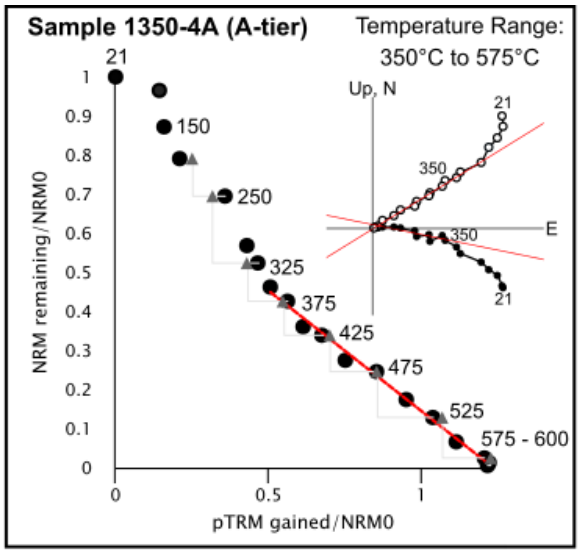
Sample 1350-4A (A-tier)
Temperature Range:
350°C to 575°C
Up, N
E
NRM remaining/NRM0
pTRM gained/NRM0
21
150
250
325
375
425
475
525
575 - 600
350

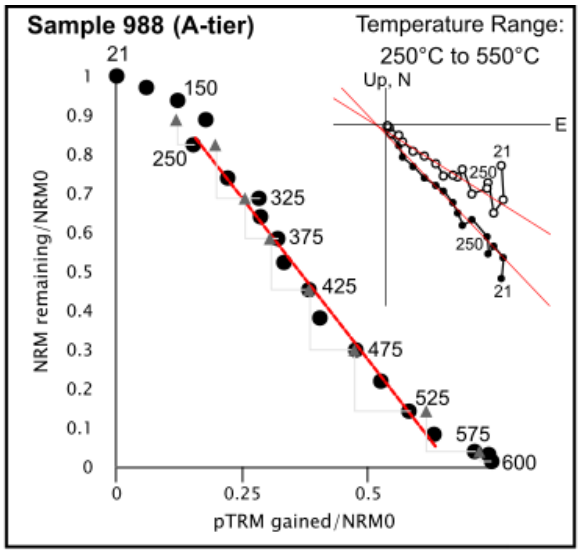
Sample 988 (A-tier)
Temperature Range:
250°C to 550°C
Up, N
E
NRM remaining/NRM0
pTRM gained/NRM0
21
150
250
325
375
425
475
525
575
600

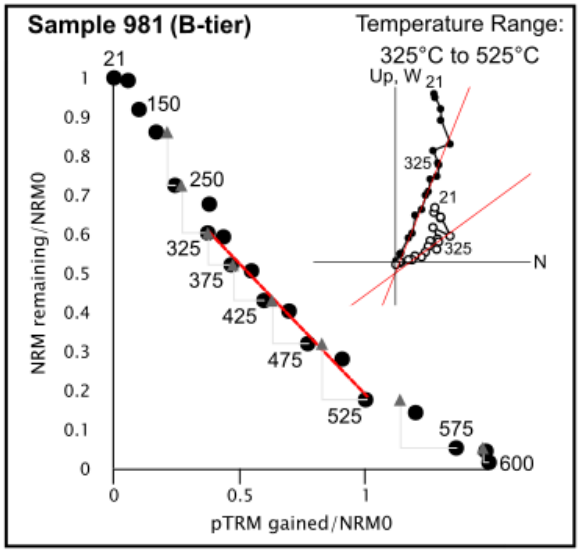
Sample 981 (B-tier)
Temperature Range:
325°C to 525°C
Up, W
N
NRM remaining/NRM0
pTRM gained/NRM0
21
150
250
325
375
425
475
525
575
600

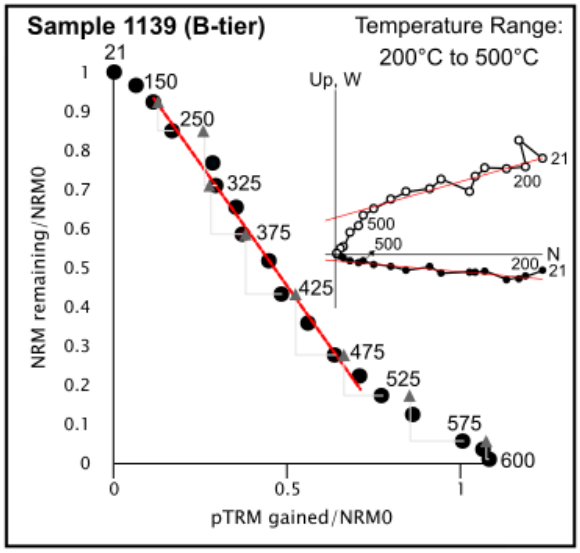
Sample 1139 (B-tier)
Temperature Range:
200°C to 500°C
Up, W
N
NRM remaining/NRM0
pTRM gained/NRM0
21
150
250
325
375
425
475
525
575
600
200
500

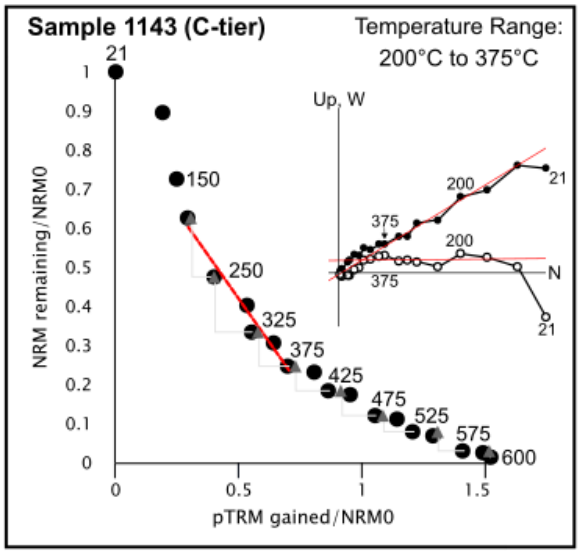
Sample 1143 (C-tier)
Temperature Range:
200°C to 375°C
Up, W
N
NRM remaining/NRM0
pTRM gained/NRM0
21
150
250
325
375
425
475
525
575
600
200

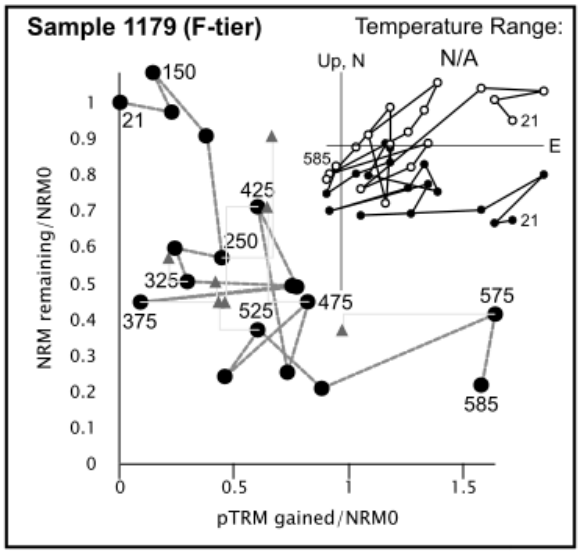
Sample 1179 (F-tier)
Temperature Range:
N/A
Up, N
E
NRM remaining/NRM0
pTRM gained/NRM0
21
150
250
325
375
425
475
525
575
585

Figure 13. Arai plots and vector endpoint diagrams for promising A, B, and C-tier sherds. Sample 1179 was the only sherd that failed all aspects of the archaeointensity experiment (F-tier). Quality tiers are explained in section 4.2. The dashed red line shows the temperature interval chosen for the primary or secondary component. Gray triangles show pTRM checks.

We classify 8 sherds as A-tier, 9 sherds as B-tier, 1 sherd as C-tier, 2 sherds as D-tier (failing 2+ criterions), and 1 sherd as F-tier (Table 4), meaning approximately 86% of sherds (A, B, and C-tier specimens) show promise for use in an ARC. Nine sherds in our quality tiers had secondary components and 13 primary components, with 4 specimens having both a promising primary and secondary component. Secondary components are of particular interest for the creation of an ARC, as these are often associated with the deposition of the radiocarbon residue used to date the sherd. The most common criteria failed by B-tier specimens was DRAT (Selkin and Tauxe, 2000), followed by f (Coe et al., 1978), |k'| (Paterson, 2011), and α (Table 4). The DRAT statistic quantifies how different pTRM checks are from the original step, the f statistic the amount of NRM used by the selected line on the Arai plot, |k'| the amount of curvature for the selected line, and α the angular difference between the anchored and free-floating best-fit directions on the vector endpoint diagram, essentially how well the magnetic component trends towards the origin. We note that temperature changes of a few degrees were common during thermal demagnetization due to the ASC oven used, which could be impacting our reported DRAT statistics.

Archaeointensities (Table 4) for A-tier, B-tier, and C-tier specimens were compared to the ARCH3k.1 (Jackson et al., 2000; Korte et al., 2009), ARCH10k.1 (Constable et al., 2016),

CALS3k.4 (Jackson et al., 2000; Korte and Constable, 2011), CALS10k.2 (Jackson et al., 2000; Constable et al., 2016), and HFM.OL1.AL1 (Panovska et al., 2015; Constable et al., 2016) global geomagnetic field models (Figure 14). Model predictions were calculated using data from the GEOMAGIA50 (Brown et al., 2015a) database and were spatially located at Minneapolis, Minnesota. The bulk of our archaeointensity estimates undershoot the models, suggesting that the global models do not capture the full range of intensity variations in Minnesota during these archaeological periods. Additionally, we note that primary component intensities are typically lower than secondary component intensities on this plot (Figure 14). Also, while samples 881-1B, 881-1C, and 881-1D are likely from different vessels, they were found at the same depth level as one another, have visually similar Arai plots, and reported very similar uncorrected archaeointensities (Table 4), suggesting they could be recording the same reheating event(s).

In an attempt to ascertain a potential correlation between sherd archaeointensity quality and magnetic properties, we compared our tier system to MDF (Figure 15a) and magnetic susceptibility (Figure 15b). Higher MDFs seem to correlate with better performance in the archaeointensity experiment, with the worst performing sample (1179) also having the smallest MDF value. Regarding susceptibility, the C-tier and D-tier specimens had marginally higher susceptibilities than the other tiers, indicating a decline in archaeointensity promise with increasing susceptibility. Though, this trend does not apply to the F-tier specimen. We also compared our tiers to specimen thickness (Figure 16a) and mass (Figure 16b). For specimen thickness there wasn't a clear relationship to sherd promise, nor was there for mass, though B-tier specimens had a much broader spread of masses than the other 4 tiers. Material characteristics of the sherds were also compared using bar charts, though due to the limited number of sherds it is difficult to pull out any reliable trends. Sherd type (rim vs. body; Figure

17a), sherd exterior treatment (cordmarked vs. plain; Figure 17b), and sherd temper (grit vs. shell; Figure 17c) did not appear to correlate to how promising a sherd was, however, we note that all 5 shell tempered sherds fell within the A and B tiers. It is emphasized, however, that our study only consisted of 21 sherds, with only 4 total making up the C, D, and F-tiers collectively, so these relationships are not robust.

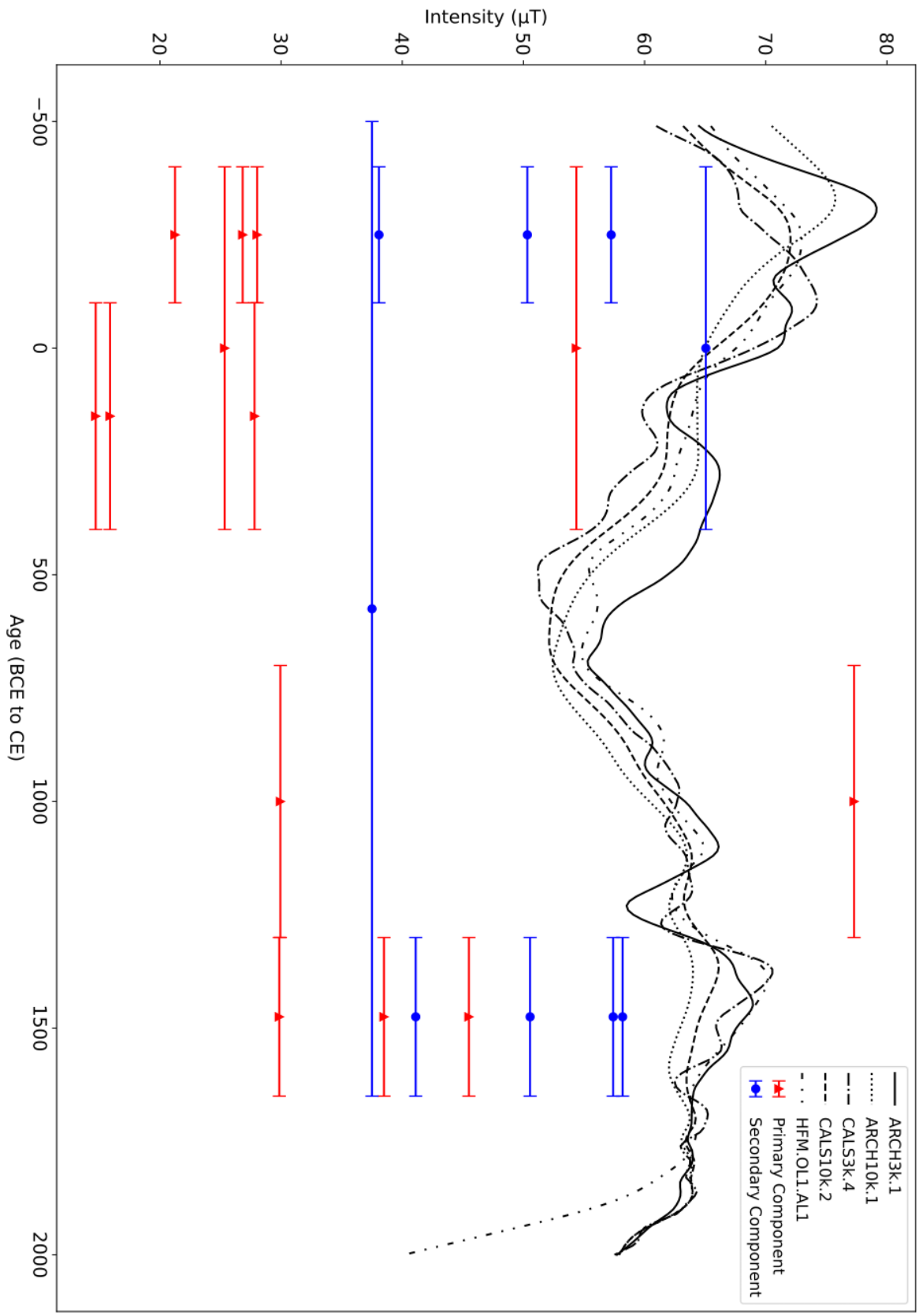
Intensity (μT)
80
70
60
50
40
30
20
−500
0
500
1000
1500
2000
Age (BCE to CE)
ARCH3k.1
ARCH10k.1
CALS3k.4
CALS10k.2
HFM.OL1.AL1
Primary Component
Secondary Component

Figure 14. Global geomagnetic field model predictions for Minnesota are calculated using the ARCH3k.1, ARCH10k.1, CALS3k.4, CALS10k.2, and HFM.OL1.AL1 models from the GEOMAGIA50 database and compared to our archaeointensities (and their material culture age ranges). The models are spatially located in Minneapolis, Minnesota. Primary components and secondary components are differentiated by red triangles and blue circles respectively.

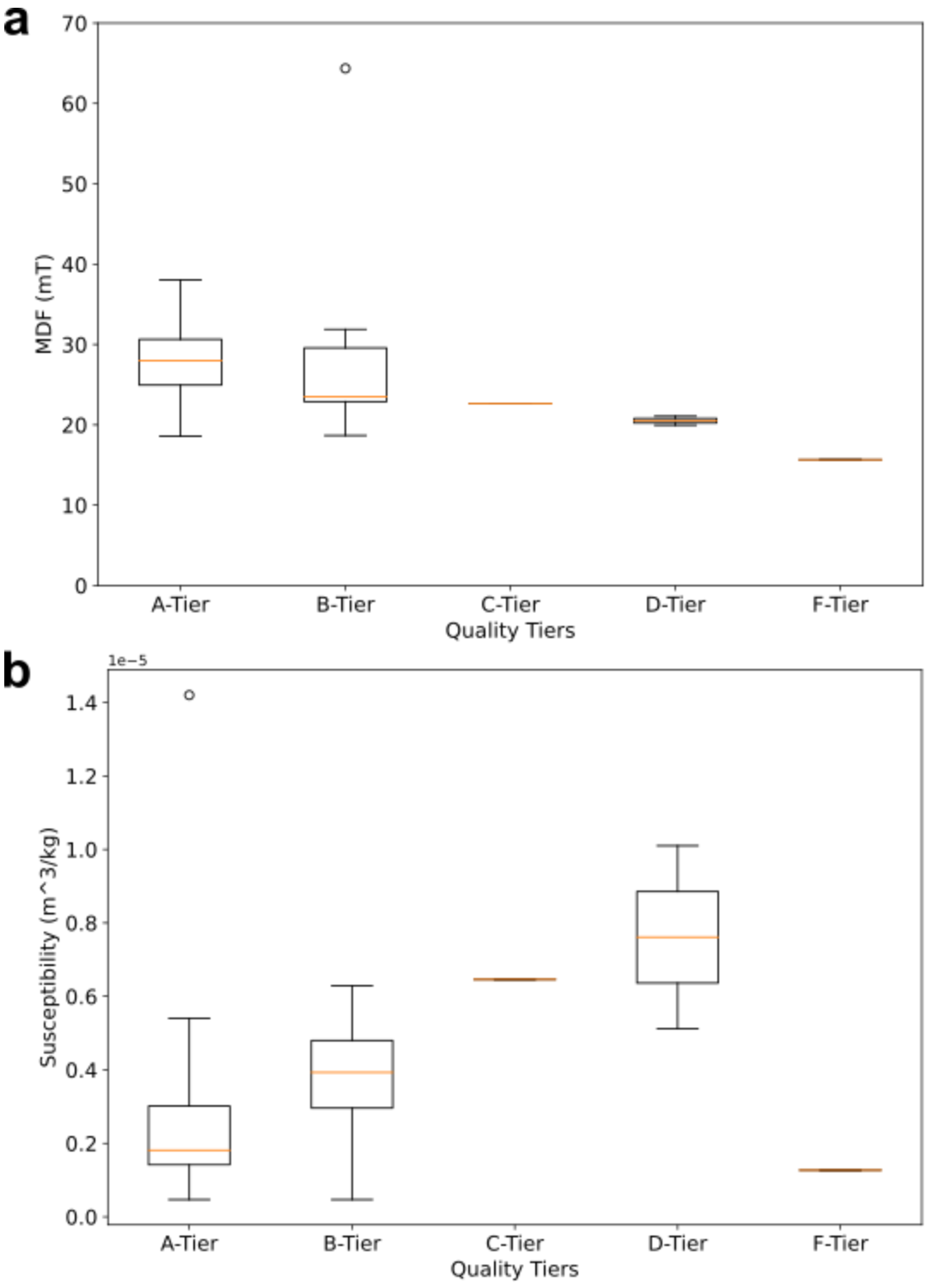

Figure 15. Box and whisker plots showing MDFs (a) and specimen susceptibility (b) organized by thermal experiment quality tiers, ranging from A (pass all selection criteria) to F (fail all

aspects of the archaeointensity experiment). Quality tiers are explained in section 4.2. Sherds in A, B, and C tiers are considered promising for the creation of an archaeomagnetic reference curve. MDFs appear to be higher for more promising samples, while susceptibility appears to be lower for more promising samples, with the exception of the F-tier sample.

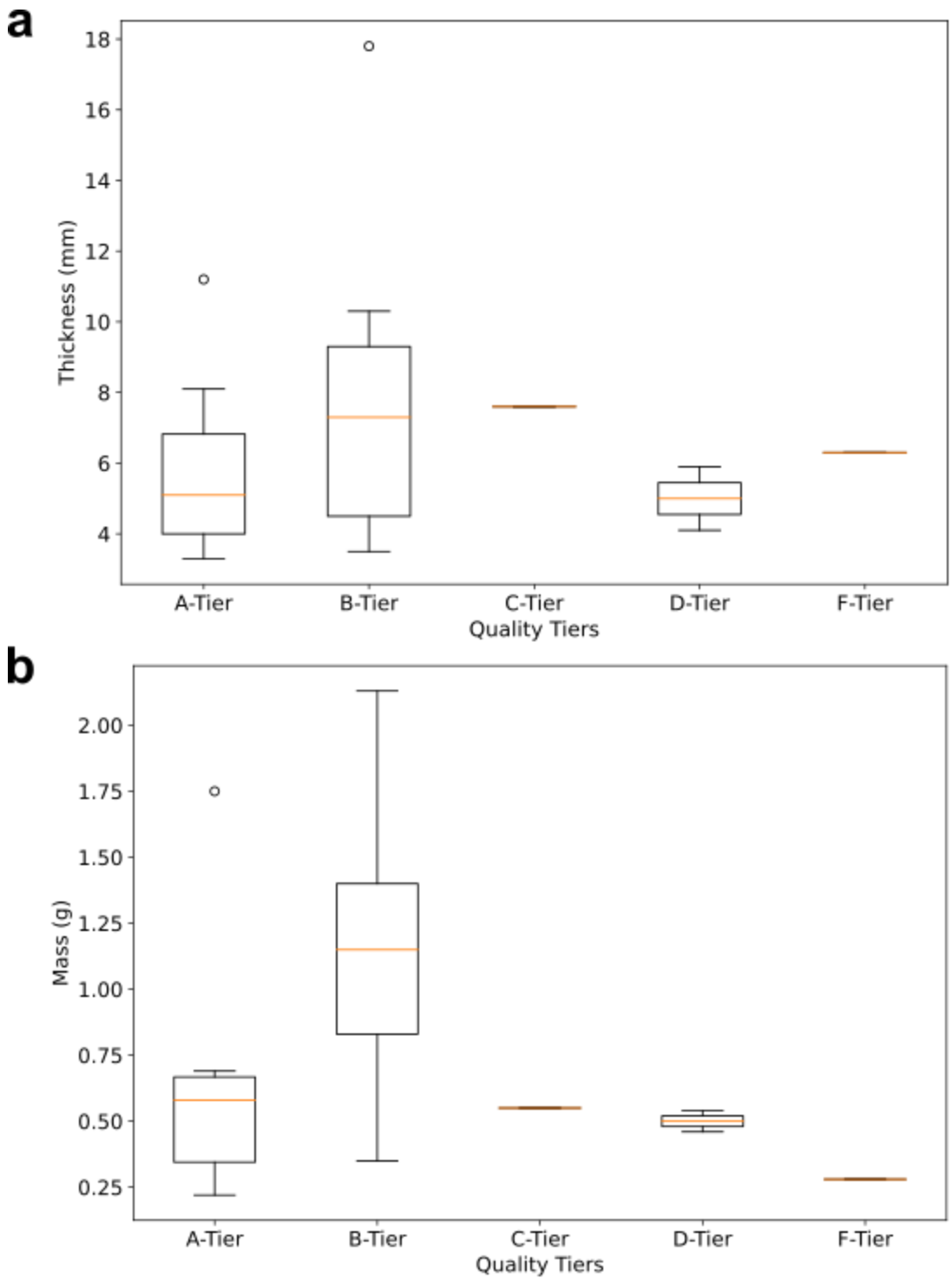

Figure 16. Box and whisker plots showing thickness (a) and specimen mass (b) organized by thermal experiment quality tiers, ranging from A (pass all selection criteria) to F (fail all aspects

of the archaeointensity experiment). Quality tiers are explained in section 4.2. Sherds in A, B, and C tiers are considered promising for the creation of an archaeomagnetic reference curve. For specimen thickness there wasn't a clear relationship to sherd promise, nor was there for mass, though B-tier specimens had a much broader spread of masses than the other 4 tiers.

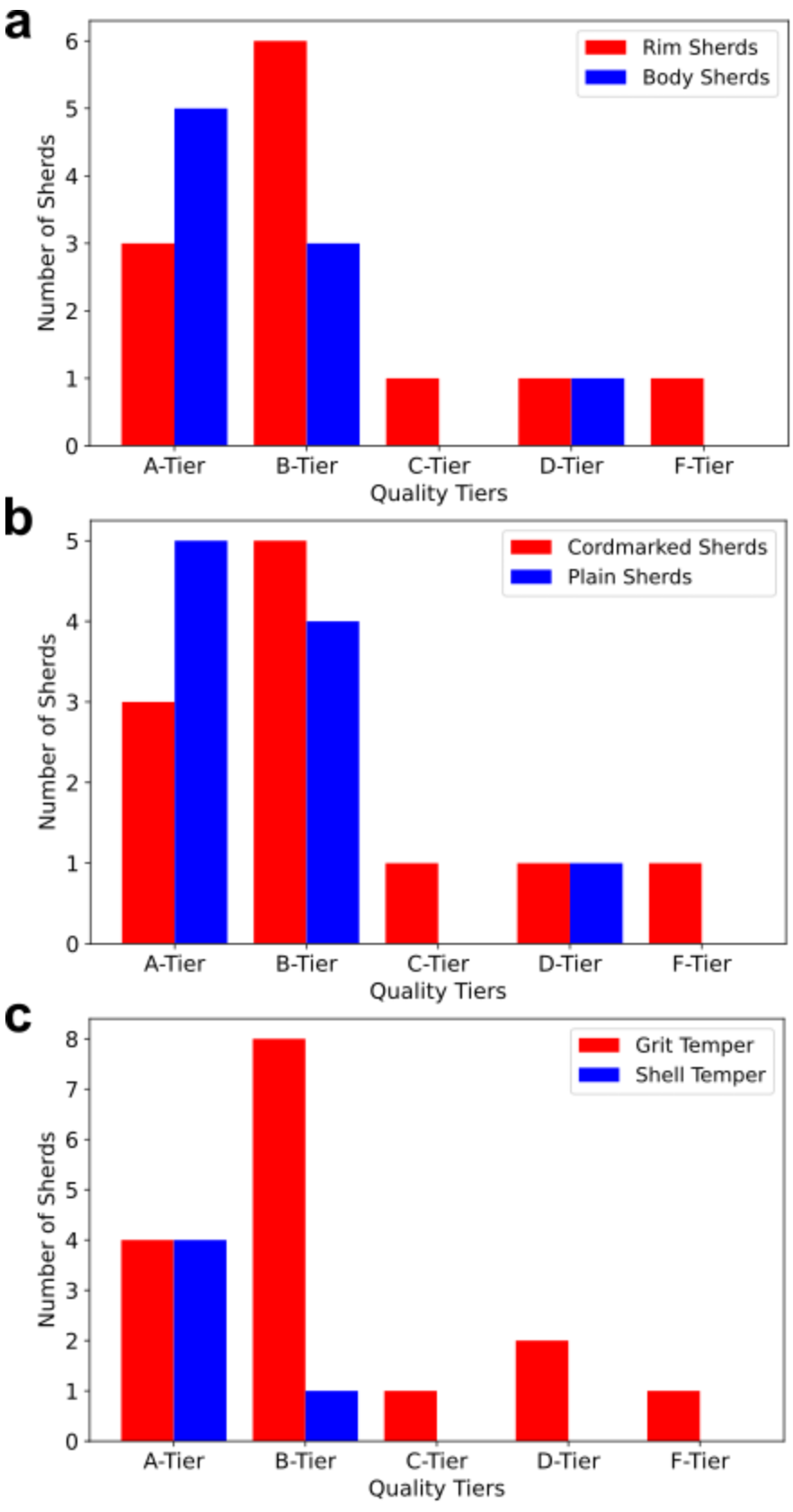
a
Rim Sherds
Body Sherds
Number of Sherds
0
1
2
3
4
5
6
A-Tier
B-Tier
C-Tier
D-Tier
F-Tier
Quality Tiers
b
Cordmarked Sherds
Plain Sherds
Number of Sherds
0
1
2
3
4
5
A-Tier
B-Tier
C-Tier
D-Tier
F-Tier
Quality Tiers
c
Grit Temper
Shell Temper
Number of Sherds
0
1
2
3
4
5
6
7
8
A-Tier
B-Tier
C-Tier
D-Tier
F-Tier
Quality Tiers

Figure 17. Bar plots showing the number of sherds in each quality tier for (a) sherd type (rim vs. body), (b) sherd exterior treatment (cordmarked vs. plain), and (c) sherd temper (grit vs. shell). Thermal experiment quality tiers range from A (pass all selection criteria) to F (fail all aspects of the archaeointensity experiment), and are explained in section 4.2. Sherds in A, B, and C tiers are considered promising for the creation of an archaeomagnetic reference curve. There does not appear to be a correlation between sherd promise and material characteristics, though we note that all 5 shell tempered sherds fell within the A and B tiers.

5. Conclusion

The main objective of this study is to determine whether or not the types of archaeological ceramics commonly found in Minnesota can be used to generate reliable archaeointensities, in service of an archaeomagnetic reference curve. Magnetic analysis of the sherds determined that the majority are dominated by mixtures of vortex and MD magnetite, with some sherds providing evidence for substantial maghemite and goethite populations. Additionally, there are rare specimens with significant hematite contributions (samples 1135 and 1350-4B), though magnetite may be overwhelming the Morin transition in other specimens.

To show the promise of Minnesota ceramics for the creation of an ARC, we considered three tiers of success: A-tier, those that fully pass modified SELCRIT2, B-tier, those that only fail one criterion, and C-tier, a single sherd that had high curvature but had a fit passing criteria. Approximately 86% of sherds were either A, B, or C-tier, showing behaviors that have potential for use in an ARC. Comparing our A-tier, B-tier, and C-tier specimens to the ARCH3k.1, ARCH10k.1, CALS3k.4, CALS10k.2, and HFM.OL1.AL1 global geomagnetic field models showed that the models may not be capturing the full range of field variations in Minnesota over our archaeological periods, an issue the MARC would be well suited to address. As our preliminary results are promising, the next phase of this project will work on creating the MARC using ceramic sherds with dateable radiocarbon residues. The MARC will allow archaeologists in the state to more precisely date heated archaeological materials, in turn providing greater precision in understanding Minnesota's chronology. Additionally, the MARC will serve the geomagnetic community by generating the data needed to better constrain geomagnetic field

models in the upper Midwest. A future publication will deal with creating the MARC and adding data to the current geomagnetic field models that describe the state.

References

2023 Fox Lake Period Ceramics. In Report on Phase 1 Research for the Handbook of Precontact Archaeological Ceramics of Minnesota, by G.R. Holley and E.P. Fleming. Report submitted to the Oversight Board of the Minnesota Statewide Archaeological Survey.

Aitken, M.J., Alcock, P.A., Bussell, G.D., and Shaw, C.J., 1981, Archaeomagnetic Determination of the Past Geomagnetic Intensity Using Ancient Ceramics: Allowance for Anisotropy: Archaeometry, v. 23, p. 53–64, doi:10.1111/j.1475-4754.1981.tb00954.x.

Anfinson, S.F., 1979, A Handbook of Minnesota prehistoric ceramics: St. Paul, Minnesota Archaeological Society, Occasional publications in Minnesota anthropology, 234 p.

Batt, C.M., Brown, M.C., Clelland, S.-J., Korte, M., Linford, P., and Outram, Z., 2017, Advances in archaeomagnetic dating in Britain: New data, new approaches and a new calibration curve: Journal of Archaeological Science, v. 85, p. 66–82, doi:10.1016/j.jas.2017.07.002.

Biggin, A.J., Perrin, M., and Dekkers, M.J., 2007, A reliable absolute palaeointensity determination obtained from a non-ideal recorder: Earth and Planetary Science Letters, v. 257, p. 545–563, doi:10.1016/j.epsl.2007.03.017.

Bilardello, D., and Egli, R., 2020, Practical Magnetism V: another FORC in the road? Understanding, measuring, and interpreting FORC diagrams, part A: The IRM Quarterly, v. 30, p. 22.

Bilardello, D., and Egli, R., 2021, Practical Magnetism VI: another FORC in the road? Understanding, measuring, and interpreting FORC diagrams, part B: The IRM Quarterly, v. 31, p. 18.

Bilardello, D., and Jackson, M., 2013, What do the Mumpsies do?: The IRM Quarterly, v. 23, p. 16.

Bowles, J., 2008, IRM gets new shielded room and u-channel magnetometer: The IRM Quarterly, v. 18, p. 8.

Brown, M.C., Donadini, F., Korte, M., Nilsson, A., Korhonen, K., Lodge, A., Lengyel, S.N., and Constable, C.G., 2015, GEOMAGIA50.v3: 1. general structure and modifications to the archeological and volcanic database: Earth, Planets and Space, v. 67, p. 83, doi:10.1186/s40623-015-0232-0.

Carvallo, C., Roberts, A.P., Leonhardt, R., Laj, C., Kissel, C., Perrin, M., and Camps, P., 2006, Increasing the efficiency of paleointensity analyses by selection of samples using first-order reversal curve diagrams: Journal of Geophysical Research: Solid Earth, v. 111, doi:10.1029/2005JB004126.

Coe, R.S., Grommé, S., and Mankinen, E.A., 1978, Geomagnetic paleointensities from radiocarbon-dated lava flows on Hawaii and the question of the Pacific nondipole low:

Journal of Geophysical Research: Solid Earth, v. 83, p. 1740–1756, doi:10.1029/JB083iB04p01740.

Constable, C., Korte, M., and Panovska, S., 2016, Persistent high paleosecular variation activity in southern hemisphere for at least 10 000 years: Earth and Planetary Science Letters, v. 453, p. 78–86, doi:10.1016/j.epsl.2016.08.015.

Chauvin, A., Garcia, Y., Lanos, Ph., and Laubenheimer, F., 2000, Paleointensity of the geomagnetic field recovered on archaeomagnetic sites from France: Physics of the Earth and Planetary Interiors, v. 120, p. 111–136, doi:10.1016/S0031-9201(00)00148-5.

Day, R., Fuller, M., and Schmidt, V.A., 1977, Hysteresis properties of titanomagnetites: Grain-size and compositional dependence: Physics of the Earth and Planetary Interiors, v. 13, p. 260–267, doi:10.1016/0031-9201(77)90108-X.

Dunlop, D.J., 2002, Theory and application of the Day plot (Mrs/Ms versus Hcr/Hc) 1. Theoretical curves and tests using titanomagnetite data: Journal of Geophysical Research: Solid Earth, v. 107, p. EPM 4-1-EPM 4-22, doi:10.1029/2001JB000486.

Fabian, K., 2003, Some additional parameters to estimate domain state from isothermal magnetization measurements: Earth and Planetary Science Letters, v. 213, p. 337–345, doi:10.1016/S0012-821X(03)00329-7.

Genevey, A., and Gallet, Y., 2002, Intensity of the geomagnetic field in western Europe over the past 2000 years: New data from ancient French pottery: Journal of Geophysical Research: Solid Earth, v. 107, p. EPM 1-1-EPM 1-18, doi:10.1029/2001JB000701.

Gibbon, G.E., 2012, Archaeology of Minnesota: The Prehistory of the Upper Mississippi River Region: University of Minnesota Press, 263 p.

Halgedahl, S.L., Day, R., and Fuller, M., 1980, The effect of cooling rate on the intensity of weak-field trm in single-domain magnetite: Journal of Geophysical Research: Solid Earth, v. 85, p. 3690–3698, doi:10.1029/JB085iB07p03690.

Harrison, R.J., and Feinberg, J.M., 2008, FORCinel: An improved algorithm for calculating first-order reversal curve distributions using locally weighted regression smoothing: Geochemistry, Geophysics, Geosystems, v. 9, doi:10.1029/2008GC001987.

Hext, G.R., 1963, The estimation of second-order tensors, with related tests and designs: Biometrika, v. 50, p. 353–373, doi:10.1093/biomet/50.3-4.353.

Jackson, A., Jonkers, A.R.T., and Walker, M.R., 2000, Four Centuries of Geomagnetic Secular Variation from Historical Records: Philosophical Transactions: Mathematical, Physical and Engineering Sciences, v. 358, p. 957–990.

Korte, M., and Constable, C., 2011, Improving geomagnetic field reconstructions for 0–3 ka: Physics of the Earth and Planetary Interiors, v. 188, p. 247–259, doi:10.1016/j.pepi.2011.06.017.

Korte, M., Donadini, F., and Constable, C.G., 2009, Geomagnetic field for 0–3 ka: 2. A new series of time-varying global models: Geochemistry, Geophysics, Geosystems, v. 10, doi:10.1029/2008GC002297.

Liu, Q., Roberts, A.P., Torrent, J., Horng, C.-S., and Larrasoaña, J.C., 2007, What do the HIRM and S-ratio really measure in environmental magnetism? Geochemistry, Geophysics, Geosystems, v. 8, doi:10.1029/2007GC001717.

Özdemir, Ö., and Dunlop, D.J., 2010, Hallmarks of maghemitization in low-temperature remanence cycling of partially oxidized magnetite nanoparticles: Journal of Geophysical Research: Solid Earth, v. 115, doi:10.1029/2009JB006756.

Panovska, S., Korte, M., Finlay, C.C., and Constable, C.G., 2015, Limitations in paleomagnetic data and modelling techniques and their impact on Holocene geomagnetic field models: Geophysical Journal International, v. 202, p. 402–418, doi:10.1093/gji/ggv137.

Paterson, G.A., Tauxe, L., Biggin, A.J., Shaar, R., and Jonestrask, L.C., 2014, On improving the selection of Thellier-type paleointensity data: Geochemistry, Geophysics, Geosystems, v. 15, p. 1180–1192, doi:10.1002/2013GC005135.

Paterson, G.A., 2011, A simple test for the presence of multidomain behavior during paleointensity experiments: Journal of Geophysical Research: Solid Earth, v. 116, doi:10.1029/2011JB008369.

Paterson, G.A., Tauxe, L., Biggin, A.J., Shaar, R., and Jonestrask, L.C., 2014, On improving the selection of Thellier-type paleointensity data: Geochemistry, Geophysics, Geosystems, v. 15, p. 1180–1192, doi:10.1002/2013GC005135.

Pick, T., and Tauxe, L., 1994, Characteristics of magnetite in submarine basaltic glass: Geophysical Journal International, v. 119, p. 116–128, doi:10.1111/j.1365-246X.1994.tb00917.x.

Roberts, A.P., Pike, C.R., and Verosub, K.L., 2000, First-order reversal curve diagrams: A new tool for characterizing the magnetic properties of natural samples: Journal of Geophysical Research: Solid Earth, v. 105, p. 28461–28475, doi:10.1029/2000JB900326.

Selkin, P.A., and Tauxe, L., 2000, Long-Term Variations in Palaeointensity: Philosophical Transactions: Mathematical, Physical and Engineering Sciences, v. 358, p. 1065–1088.

Shaar, R., Tauxe, L., Ron, H., Ebert, Y., Zuckerman, S., Finkelstein, I., and Agnon, A., 2016, Large geomagnetic field anomalies revealed in Bronze to Iron Age archeomagnetic data from Tel Megiddo and Tel Hazor, Israel: Earth and Planetary Science Letters, v. 442, p. 173–185, doi:10.1016/j.epsl.2016.02.038.

Stillinger, M.D., Feinberg, J.M., and Frahm, E., 2015, Refining the archaeomagnetic dating curve for the Near East: new intensity data from Bronze Age ceramics at Tell Mozan, Syria: Journal of Archaeological Science, v. 53, p. 345–355, doi:10.1016/j.jas.2014.10.025.

Tauxe, L, Banerjee, S.K., Butler, R.F. and van der Voo R, Essentials of Paleomagnetism, 5th Web Edition, 2018.

Tauxe, L., Mullender, T. a. T., and Pick, T., 1996, Potbellies, wasp-waists, and superparamagnetism in magnetic hysteresis: Journal of Geophysical Research: Solid Earth, v. 101, p. 571–583, doi:10.1029/95JB03041.

Tauxe, L., and Staudigel, H., 2004, Strength of the geomagnetic field in the Cretaceous Normal Superchron: New data from submarine basaltic glass of the Troodos Ophiolite: Geochemistry, Geophysics, Geosystems, v. 5, doi:10.1029/2003GC000635.

Tauxe, L., Shaar, R., Jonestrask, L., Swanson-Hysell, N.L., Minnett, R., Koppers, A. a. P., Constable, C.G., Jarboe, N., Gaastra, K., and Fairchild, L., 2016, PmagPy: Software package for paleomagnetic data analysis and a bridge to the Magnetics Information Consortium (MagIC) Database: Geochemistry, Geophysics, Geosystems, v. 17, p. 2450–2463, doi:10.1002/2016GC006307.

Thellier, E., and Thellier, O., 1959, Sur l'intensité du champ magnétique terrestre dans le passé historique et géologique: Annales de Geophysique, v. 15, p. 285.

Thompson, R., and Oldfield, F., 1986, Environmental Magnetism: Springer Dordrecht, 228 p.

Zijderveld, J.D.A., 2013, A. C. Demagnetization of Rocks: Analysis of Results, in Collinson, D.W., Creer, K.M., and Runcorn, S.K. eds., Developments in Solid Earth Geophysics, Elsevier, Methods in Palaeomagnetism, v. 3, p. 254–286, doi:10.1016/B978-1-4832-2894-5.50049-5.

Appendix A. Tables

Table A1. Sherd Material Characteristics and Ages

Sample ID	Sherd Type	Surface Treatment	Decoration	Temper	Phase	Time Range	Thickness (mm)	Sample Mass (g)
A73-7-1079	Rim	Cordmarked (horizontal) ext	Boss, Interior lip decoration - angled parallel incised lines	Grit	Fox Lake, horizontal cordmarked	ca. 400 - 100 BCE	7.8	10.9
A73-7-1135	Rim	Cordmarked (horizontal) ext	None	Grit	Fox Lake	ca. 400 - 100 BCE	11.2	13.2
A73-7-1139	Rim	Cordmarked (exterior)	Incised lines (exterior), Boss (exterior), cordwrapped stick-impressed (interior)	Grit	Fox Lake, incised	ca. 400 - 100 BCE	10.3	4.5
A73-7-1143	Rim	Cordmarked (exterior)	Cordwrapped stick-impressed (interior)	Grit	Vertical cordmarked (Hudak Type C)	Undetermined (500 BCE - 1650 CE)	7.6	2.0
A73-7-1179	Rim	Cordmarked (exterior)	None	Grit	Lake Benton	ca. 700 - 1200/1300 CE	6.3	1.4
A73-7-1220	Rim	Cordmarked (exterior), Exfoliated (interior)	None	Grit	Lake Benton	ca. 700 - 1200/1300 CE	3.5	1.0
A73-7-1325	Rim	Plain (exterior)	Cordwrapped stick stamped (exterior)	Grit	Lake Benton faint stamped	ca. 700 - 1200/1300 CE	5.9	1.6
A73-7-1350-4A	Body	Plain	None	Grit	non-diagnostic	ca. 500 BCE - 500 CE	8.1	6.4
A73-7-1350-4B	Body	Plain	None	Grit	non-diagnostic	ca. 1300 - 1650 CE	4.5	2.8
A73-7-1350-7A	Body	Cordmarked (exterior)	None	Grit	non-diagnostic	ca. 500 BCE - 500 CE	9.3	5.6
A73-7-	Body	Cordmarked	None	Grit	non-	ca. 500 CE - 1300	4.1	2.1

1350-7B		(exterior)			diagnostic	CE		
A73-7-441	Rim	Plain (exterior), Exfoliated (interior)	Cordwrapped stick-impressed (exterior)	Grit	Temperance Lake (Hudak Type A)	ca. 100 BCE - 400 CE	6.4	3.0
A73-7-858-3	Body	Cordmarked (exterior)	None	Shell	Poss. Sandy Lake	ca. 1300 - 1650 CE	5.9	2.3
A73-7-881-1A	Body	Plain	None	Shell	Oneota	ca. 1300 - 1650 CE	4.3	1.5
A73-7-881-1B	Body	Plain	None	Shell	Oneota	ca. 1300 - 1650 CE	3.3	1.3
A73-7-881-1C	Body	Plain	None	Shell	Oneota	ca. 1300 - 1650 CE	4.0	1.2
A73-7-881-1D	Body	Plain	None	Shell	Oneota	ca. 1300 - 1650 CE	4.0	0.6
A73-7-981	Rim	Plain (exterior)	Cordwrapped stick-impressed (exterior)	Grit	Temperance Lake (Hudak type A)	ca. 100 BCE - 400 CE	17.8	7.6
A73-7-985	Rim	Cordmarked (exterior)	None	Grit	Fox Lake, horizontal cordmarked	ca. 400 - 100 BCE	7.3	4.5
A73-7-988	Rim	Cordmarked (exterior), Exfoliated (interior)	None	Grit	Lake Benton	ca. 700 - 1200/1300 CE	4.3	1.0
A74-5-573-6	Rim	Plain (exterior)	Cordwrapped stick-impressed (exterior)	Grit	Temperance Lake	ca. 100 BCE - 400 CE	6.4	2.2

Table 1. Sherd material characteristics, ceramic phases, and time ranges. The Fox Lake and Temperance Lake age ranges are estimates from Holley (2023), the Lake Benton age range is from Anfinson (1997), and the nondiagnostic likely age ranges are from Gibbon (2012). Sample mass was taken prior to separation of the sherds into specimens, the mass of the fragments (specimens) was later taken and used for subsequent analyses.

Table A2. Thermal Selection Criteria

	Thermal Criteria
Criterion	**Modified SELCRIT2**
n	≥ 4
f	≥ 0.35
β	≤ 0.1
q	≥ 1
MAD_{Anc}	≤ 15
α	≤ 15
DRAT	≤ 10
|k'|	$\leq .164$

Table 2. Criterions for the modified SELCRIT2 thermal selection criteria (Biggin et al., 2007; Paterson et al., 2014). n is the number of data points used to establish the best-fit line used to calculate the archaeointensity, f the amount of NRM used by the selected line on the Arai plot, β the scatter about the best-fit line used, q the quality of the archaeointensity estimate (combining the relative scatter of the best-fit line, the NRM fraction, and a gap factor), MADAnc the maximum angular deviation of the anchored best-fit direction on the vector endpoint diagram, α the angular difference between the anchored and free-floating best-fit directions on the vector endpoint diagram, DRAT a measure of how different pTRM checks are from the original step, and |k'| a measure of the amount of curvature for the selected best-fit line. These definitions are explained in and sourced from Standard Paleointensity Definitions v1.2.0 (Paterson et al., 2014).

Table A3. Rock Magnetic Results

Sample	NRM of Thermal Specimen [mAm^2/kg]	Mr/Ms	Bcr/Bc	S300	HIRM [mAm^2/kg]	Sigma	MDF [mT]	FWHM [mT]	Mean Total Susceptibility [$\mu m^3/kg$]
A73-7-1079	1.40	0.11	3.7	0.99	5.24E-02	-0.04	22.9	3.1	7.08
A73-7-1135	3.39E-02	0.06	9.6	0.63	6.20E-01	0.38	38.2	8.5	8.11E-01
A73-7-1139	8.03E-01	0.09	3.8	0.98	1.74E-01	-0.09	20.3	4.9	5.41
A73-7-1143	6.20E-01	0.10	4.1	0.98	2.25E-01	-0.05	22.7	4.5	6.36
A73-7-1179	3.19E-02	0.01	12.2	0.96	3.40E-02	-0.06	28.8	16.6	1.24
A73-7-1220	7.54E-01	0.14	3.2	0.98	1.63E-01	-0.05	29.6	5.4	4.11
A73-7-1325	3.48E-01	0.11	3.1	1.00	**ERROR**	-0.14	20.0	4.5	4.56
A73-7-1350-4A	1.06	0.16	3.0	0.98	2.71E-01	-0.07	28.0	4.5	5.56
A73-7-1350-4B	1.03E-01	0.15	4.0	0.85	4.34E-01	0.02	64.4	15.5	3.36E-01
A73-7-1350-7A	1.36	0.19	2.5	0.94	5.63E-01	-0.003	29.1	6.3	2.50
A73-7-1350-7B	7.58E-01	0.05	4.3	0.99	4.35E-02	-0.25	21.1	7.6	7.82

A73-7-441	4.69E-02	0.04	6.5	0.95	5.62E-02	-0.06	23.2	6.7	1.28
A73-7-858-3	8.61E-02	0.09	4.0	0.96	3.04E-02	-0.07	23.7	5.8	5.28E-01
A73-7-881-1A	8.82E-01	0.14	3.5	0.94	5.44E-01	0.03	23.5	3.1	3.67
A73-7-881-1B	4.31E-01	0.14	3.4	0.91	7.32E-01	-0.05	30.3	4.0	1.75
A73-7-881-1C	4.09E-01	0.12	3.8	0.92	5.24E-01	-0.07	28.0	2.2	1.83
A73-7-881-1D	5.86E-01	0.14	3.4	0.92	7.66E-01	-0.07	31.6	4.0	1.39
A73-7-981	4.78E-01	0.06	4.6	0.97	1.63E-01	-0.19	31.9	5.4	3.61
A73-7-985	3.56E-01	0.05	5.0	0.98	8.35E-02	-0.14	18.7	3.6	5.04
A73-7-988	1.87	0.09	3.6	0.99	1.09E-01	-0.14	18.6	5.0	12.3
A74-5-573-6	2.35E-01	0.07	5.2	0.91	4.51E-01	-0.09	43.5	6.7	2.02

Table 3. Rock magnetic experiment results. Mr/Ms and Bcr/Bc ratios are plotted on the Day plot (see section 4.1.1. and Figure 5). S-ratios (S300) and HIRMs are discussed in section 4.1.2., sigmas and FWHMs in section 4.1.1., and MDFs and susceptibility (Figure 4) in section 4.1. Sample 1325 had an S300 value slightly greater than 1 (1.00118) and a negative HIRM value, likely due to instrumental error.

Table A4. Archaeointensity Results

							Parameter Values							
Sample	**Quality Tier**	**Temp Range**	**Uncorrected Intensity (μT)**	**Cooling Rate Correction Factor**	**Anisotropy Correction Factor**	**Corrected Intensity (μT)**	**n**	**f**	**β**	**q**	**|k'|**	**MAD_{Anc}**	**α**	**DRAT**
A73-7-1079	B	**Primary:** 475°C - 600°C	28.2	0.94	1.06	28.0	7	0.366	0.048	6.1	0.024	4.9	5.3	***15.1***
A73-7-1079	B	**Secondary:** 250°C - 450°C	51.2	0.94	1.05	50.3	8	0.405	0.094	3.6	0.140	3.1	8.9	4.1
A73-7-1135	A	**Secondary:** 100°C - 350°C	44.6	0.85	-	38.1*	7	0.627	0.042	12.3	0.069	9.4	13.6	4.1
A73-7-1139	B	**Primary:** 500°C - 600°C	21.4	0.94	1.06	21.2	6	***0.347***	0.049	5.3	0.115	4.6	3.9	***20.8***
A73-7-1139	B	**Secondary:** 200°C - 500°C	50.0	0.94	1.22	57.2	11	0.672	0.039	15.5	0.058	6.5	14.8	9.8
A73-7-1143	C	**Secondary:** 200°C - 375°C	35.9	0.93	1.12	37.5	6	0.431	0.098	3.4	0.158	4.5	8.2	5.1
A73-7-1179	F	N/A	-	-	-	-	-	-	-	-	-	-	-	-
A73-7-1220	B	**Primary:** 525°C - 600°C	23.2	0.92	1.40	30.0	5	0.351	0.041	6.3	0.010	5.4	5.0	***15.8***
A73-7-1325	D	N/A	-	-	-	-	-	-	-	-	-	-	-	-
A73-7-1350-4A	A	**Primary:** 350°C - 600°C	24.7	0.96	1.07	25.3	12	0.587	0.023	22.8	0.070	4.0	2.0	4.9
A73-7-1350-4B	B	**Primary:** 425°C - 585°C	32.3	0.91	1.02	29.9	8	0.558	0.055	8.5	0.164	4.8	5.8	***13.4***

A73-7-1350-7A	B	**Primary:** 475°C - 575°C	51.0	0.92	1.16	54.4	5	0.466	0.046	7.4	***0.218***	7.1	3.0	5.7
A73-7-1350-7A	B	**Secondary:** 250°C - 475°C (excluding 375°C pTRM check)	71.2	0.92	0.99	65.1	9	0.427	0.027	13.7	0.056	6.4	***18.5***	1.8
A73-7-1350-7B	D	N/A	-	-	-	-	-	-	-	-	-	-	-	-
A73-7-441	B	**Primary:** 450°C - 585°C	18.1	0.88	0.99	15.9	7	0.359	0.077	3.8	0.012	6.0	3.0	***18.5***
A73-7-858-3	A	**Primary:** 350°C - 525°C	36.4	0.91	1.37	45.5	8	0.407	0.030	11.6	0.044	6.6	7.7	7.8
A73-7-881-1A	B	**Primary:** 525°C - 600°C	38.2	0.93	1.09	38.5	5	***0.242***	0.051	3.3	0.145	1.5	1.5	8.7
A73-7-881-1A	B	**Secondary:** 100°C - 450°C (excluding 250°C)	43.9	0.93	1.24	50.6	10	0.564	0.031	15.4	0.093	9.9	***27.6***	1.5
A73-7-881-1B	A	**Secondary:** 100°C - 350°C (excluding 200°C)	62.2	0.94	***8.28***	58.2*	6	0.794	0.045	13.4	0.037	10.1	13.7	0.1
A73-7-881-1C	A	**Secondary:** 150°C - 375°C	61.4	0.91	0.74	41.1	7	0.818	0.028	23.8	0.110	5.8	8.1	6.3
A73-7-881-1D	A	**Secondary:** 100°C - 375°C	61.4	0.92	1.02	57.4	8	0.823	0.058	11.7	0.096	8.7	13.2	3.6
A73-7-981	B	**Primary:** 325°C - 525°C	26.9	0.93	1.12	27.8	9	0.495	0.059	7.3	0.076	2.9	5.8	7.1

A73-7-985	B	**Primary :** 350°C - 550°C	25.9	0.93	1.11	26.8	9	0.568	0.039	12.6	***0.276***	3.0	2.8	9.7
A73-7-988	A	**Primary :** 250°C - 550°C	66.2	0.94	1.24	77.3	12	0.697	0.037	17.2	0.103	4.2	3.5	6.4
A74-5-573-6	A	**Primary :** 375°C - 575°C	24.0	0.95	0.69	14.7	9	0.593	0.026	20.0	0.094	5.4	7.1	8.2

Table 4. Specimen archaeointensity results. Quality tiers range from A (pass all selection criteria) to F (which fail all aspects of the archaeointensity experiment). Quality tiers are explained in section 4.2. Primary and secondary temperature ranges are the temperatures over which primary and secondary components are identified, with intensities corrected using factors from anisotropy and cooling rate experiments (sections 3.2.2. and 3.2.3.). For samples with an asterisk (*) on the corrected intensity we either could not complete an anisotropy experiment (1135) or received an inflated value (881-1B), so these samples are only corrected for cooling rate (see section 3.2.2.). Samples 1350-7B, 881-1C, and 573-6 were corrected using an AARM experiment instead of an ATRM experiment (section 3.2.2.). Parameter values are from modified SELCRIT2 (Biggin et al., 2007; Paterson et al., 2014; Table 3), with criterions that failed bolded and italicized.

Table A5. F-Test Results

Sample	F-Test	Number of Positions	Critical F Value	Result Quality
A73-7-1079	1.69	6	3.1059	b
A73-7-1135	-	-	-	-
A73-7-1139	0.60	6	3.1059	b
A73-7-1143	6.64	6	3.1059	g
A73-7-1179	-	-	-	-
A73-7-1220	5.48	6	3.1059	g
A73-7-1325	57.48	6	3.1059	g
A73-7-1350-4A	0.51	6	3.1059	b
A73-7-1350-4B	1.62	6	3.1059	b
A73-7-1350-7A	4.19	6	3.1059	g
A73-7-1350-7B	-	-	-	-
A73-7-441	1.67	6	3.1059	b
A73-7-858-3	1.87	6	3.1059	b
A73-7-881-1A	1.01	6	3.1059	b
A73-7-881-1B	0.0047	6	3.1059	b
A73-7-881-1C	0.0019	6	3.1059	b
A73-7-881-1D	3.78	6	3.1059	g
A73-7-981	14.62	6	3.1059	g
A73-7-985	0.46	6	3.1059	b
A73-7-988	3.50	6	3.1059	g
A74-5-573-6	0.0045	6	3.1059	b

Table 5. F-Test (Hext, 1963) results from Thellier GUI (Tauxe et al., 2016). Six positions were used, necessitating a critical F value of 3.1059. Seven of the eighteen specimens subjected to an anisotropy correction had F-test values that exceeded the critical F-value. Result quality is listed as “b” or “g,” referring to bad and good. A specimen is marked as good if its F-test value exceeded the critical value. F-tests for samples 1350-7B, 881-1C, and 573-6 are from an AARM experiment, with all other F-tests are from ATRM experiments (section 3.2.2.). Specimen 881-1B had an inflated anisotropy correction factor (8.28).